

Effect of Electron Precipitation on E-Region Instabilities: Theoretical Analysis

Y. S. Dimant¹, G. V. Khazanov², and M. M. Oppenheim¹

¹Center for Space Physics, Boston University, Boston, MA USA

²NASA Goddard Space Flight Center, Greenbelt, MD USA

Key Points:

- During geomagnetic storms, strong electric fields and intense electron precipitation may overlap in the E-region ionosphere, where magnetospheric currents close.
- Without precipitation, sufficiently strong electric fields drive E-region instabilities, leading to plasma turbulence and increased ionospheric conductance.
- The intense electron precipitation may raise dramatically the instability threshold, largely suppressing the instability inside the auroral regions.

arXiv:2107.04692v1 [physics.space-ph] 9 Jul 2021

Abstract

During periods of strong geomagnetic activity, intense currents flow from the magnetosphere into the high-latitude E-region ionosphere along geomagnetic field lines, B . In this region, collisions between the plasma and neutral molecules allow currents to flow across B , enabling the entire magnetosphere-ionosphere current system to close. These same currents cause strong DC electric fields in the E-region ionosphere where they drive plasma instabilities, including the Farley-Buneman instability (FBI). These instabilities give rise to small-scale plasma turbulence that modifies the large-scale ionospheric conductance that, in turn, affects the evolution of the entire near-Earth plasma environment. Also, during geomagnetic storms, precipitating electrons of high energies, $\gtrsim 5$ keV, frequently penetrate down to the same regions where intense currents and E fields develop. This research examines the effects of precipitating electrons on the generation of the FBI and shows that, under many common conditions, it can easily suppress the FBI in a predictable manner. Applying the kinetic SuperThermal Electron Transport (STET) code, we have analyzed the distribution function expected in the E-region and the effects of these energetic electron distributions on the FBI onset criterion. This shows that the plasma pressure of superthermal electrons may be comparable to, or even significantly exceed, the regular plasma pressure of the cold ionospheric plasma. This will increase the FBI threshold and suppress the instability in auroral regions. However, our detailed theoretical analysis shows that the effect of the superthermal precipitating electrons is much stronger than just the effect of the additional pressure. We were surprised to discover that the energy dependence of the electron-neutral collision frequency can greatly enhance the effect of this additional pressure, further suppressing the FBI, even at a moderate precipitation level. Therefore, we expect precipitation to exert a significant feedback on the magnetosphere by preventing the elevated conductivity caused by FBI driven turbulence. This suppression should be taken into account in global modeling of the magnetosphere-ionosphere coupling.

1 Introduction

During periods of intense geomagnetic activity, strong DC electric fields, \vec{E}_0 , perpendicular to the geomagnetic field, \vec{B} , penetrate from the Earth's magnetosphere into the high-latitude ionosphere where they dissipate energy, form electrojets, and drive plasma instabilities in the E-region ionosphere, at altitudes roughly between 90 and 120 km. In the global picture of magnetosphere-ionosphere coupling, this is the region where most of the field-aligned magnetospheric currents close. The E-region instabilities generate plasma density irregularities, typically within the wavelength range from tens of centimeters to tens of meters, coupled with wavelike electrostatic field fluctuations. The density irregularities have been routinely detected as strong coherent radar echoes (e.g., Bahcivan et al., 2005, 2006; Hysell et al., 2008; Forsythe & Makarevich, 2015). The electrostatic field fluctuations have been detected by rocket flights through the lower ionosphere (Pfaff et al., 1984, 1987, 1992, 1997; Rose et al., 1992; Fukao et al., 1998). The E-region instabilities include the Farley-Buneman (Farley, 1963; Buneman, 1963), gradient drift (Hoh, 1963; Maeda et al., 1963), and thermal instabilities (e.g., Dimant & Sudan, 1997; Dimant & Oppenheim, 2004; M. Oppenheim et al., 2020, and references therein). The strongest among all E-region instabilities, the Farley-Buneman instability (FBI), is excited when the relative speed between the average electron and ion streams exceeds the local ion-acoustic speed. At high latitudes, this usually occurs when $|\vec{E}_0| \gtrsim 20$ mV/m. This and much stronger fields are not uncommon in the subauroral, auroral, and polar cap areas, especially during geospace storms and substorms. Driven by magnetospheric activities, small-scale E-region instabilities heat electrons (e.g., Foster & Erickson, 2000; Milikh & Dimant, 2003; M. M. Oppenheim & Dimant, 2013, and references therein) and may affect ionospheric conductivities, which in turn exert large-scale feedback on the magnetosphere (Merkin et al., 2005; Dimant & Oppenheim, 2011; Wiltberger et al., 2017).

At the same time, high-latitude regions are characterized by strong electron precipitation that gives rise to such spectacular phenomena as Aurora Borealis. The electron energy distribution in the aurora displays many different forms that are usually described by qualitative criteria developed by Newell et al. (2009). The majority of these electron energy distributions are classified as diffuse, monoenergetic, or broadband. In Section 2.2, we provide a detailed description of different kinds of aurora.

In this paper, we focus on auroral regions where intense electron precipitation may overlap with strong driving DC fields. We study the distribution function modifications caused by precipitating electrons and the effect of these modifications on the instability development. Using a physics-based model of electron precipitation from the STET model described below, we study how this precipitation affects the E-region instability criterion.

We show that precipitating electrons of sufficiently high energies, $E_0 \gtrsim 5$ keV, can easily penetrate down to the E-region. The plasma turbulence associated with the E-region instabilities does not have sufficient energy to exert noticeable feedback on the behavior of precipitating electrons, however this paper shows that the reverse may be quite common. We show this by using the kinetic linear theory of the FBI and estimating the effect of precipitating superthermal electrons (SE) on its onset criterion.

The paper is organized as follows. In section 2, we discuss in general the E-region instabilities (section 2.1), as well as electron precipitation and the kinetic tool to treat the latter (section 2.2). In section 3, we present the results of our kinetic simulations using STET. Section 4 is the central section of the paper, where we present our theoretical analysis. To obtain a useful insight into the possible effect of superthermal electrons on the FBI, we start with an oversimplified three-fluid analysis (section 4.1). Then, in section 4.2, we present our principal theoretical analysis based on a hybrid approach (an approximate kinetic theory for electrons combined with the fluid model of ions). In section 4.3, using the results of our kinetic simulations described in section 3, we give simple estimates of the modified instability threshold in the presence of superthermal electrons. In section 5, we give the conclusions and the final discussion. In the appendices, we give some details of analytic approximations of the collision cross-section and distribution function.

2 Background

2.1 Outline of the FBI Onset

Here we briefly describe the FBI linear theory relevant to our topic. All E-region instabilities occur within the lower altitude range of the ionosphere where electrons are strongly magnetized, $\omega_{ec} \gg \nu_{en}$, while ions are fully or partially unmagnetized due to their frequent collisions with neutral atmospheric molecules, $\omega_{ic} \lesssim \nu_{in}$, where ω_{ec} and ω_{ic} are the electron and ion cyclotron frequencies; ν_{en} and ν_{in} are the electron-neutral (e - n) and ion-neutral (i - n) mean collision frequencies, respectively (for simplicity, we assume only single-species ions). The mean collision frequencies are altitude-dependent parameters averaged over the entire particle distributions. To avoid a confusion, we note that in the kinetic description of electrons (section 4) we will use the same notation for the velocity-dependent e - n collision frequency, $\nu_{en}(V_e)$ (the reader should pay attention to the context). At high latitudes, the above conditions usually hold at E-region altitudes between 90 and 120 km.

All E-region instabilities excite low-frequency plasma-density compression/rarefaction waves. Though such waves are usually acoustic-like, no long-lived ion acoustic waves can exist in the highly dissipative E-region ionosphere. Long-lived plasma waves persist there only due to an external DC electric field, $\vec{E}_0 \perp \vec{B}$. These plasma waves are quasineutral, where weak charge separation gives rise to coupled electrostatic field oscillations.

The frequencies of these excited waves, ω , are typically lower than the characteristic collision frequencies, $\omega \lesssim \nu_{in} \ll \nu_{en}$, while the typical wavelengths are larger than the i - n collisional mean free path. The corresponding wavevectors, \vec{k} , are largely perpendicular to \vec{B} . In the perpendicular to \vec{B} plane, depending on the driving-field magnitude, E_0 , the wavevectors are mostly directed within a cone of a few tens of degrees wide around the electron $\vec{E}_0 \times \vec{B}$ -drift velocity, $\vec{V}_0 = \vec{E}_0 \times \vec{B}/B^2$, where $B = |\vec{B}|$.

If the particle velocity distributions are close to Maxwellian then, for sufficiently long-wavelength waves (see below), the linear stage of the FBI and other E-region instabilities can be reasonably well described by a closed set of five-moment fluid-model equations that includes the continuity equation, the momentum, and the energy balance equations (e.g., Dimant & Oppenheim, 2004):

$$\frac{\partial n_s}{\partial t} + \nabla \cdot (n_s \vec{V}_s) = 0, \quad (1a)$$

$$m_s \frac{D_s \vec{V}_s}{Dt} = q_s (\vec{E} + \vec{V}_s \times \vec{B}) - \frac{\nabla P_s}{n} - m_s \nu_{sn} \vec{V}_s, \quad (1b)$$

$$n_s^{3/2} \frac{D_s}{Dt} \left(\frac{T_s}{n_s^{3/2}} \right) = \frac{2}{3} M_{sn} \nu_{sn} V_s^2 - \delta_{sn} \nu_s (T_s - T_n). \quad (1c)$$

Here the subscript $s = e, i$ characterizes a specific plasma fluid; $D_s/Dt \equiv \partial_s/\partial t + \vec{V}_s \cdot \nabla$; \vec{V}_s , m_s , q_s , and T_s are the s -particle mean flow velocities, particle masses, charges ($q_i = e$, $q_e = -e$), and temperatures (in energy units); $V_s = |\vec{V}_s|$; m_n and T_n are the neutral mass and temperature, respectively; $P_s \approx n_s T_s$ is the s -fluid pressure; $M_{sn} = m_s m_n / (m_s + m_n)$ is the effective mass of the two colliding particles (s and n); and δ_{sn} is the average fraction of energy lost by the particle of the s -species during one s - n collision; here $\delta_{in} \simeq 1$ and $\delta_{en} \simeq (2-4) \times 10^{-3}$ (Gurevich, 1978). Equation (1) implies the frame of reference attached to the mean neutral flow.

In equation (1), we assume a single ion (i) species because the two major E-region ion components, O_2^+ and NO_2^+ , have fairly close masses ($m_i \simeq 30 m_p$, where m_p is the proton mass) and comparable collision frequencies; the same can be assumed for neutrals (n). Note that this simplified set of moment equations misses a few factors, e.g., ionization-recombination, anisotropic pressure, viscosity, and heat conductivity, which play little to no role in E-region waves.

For the E-region processes, the two sets of the moment equations for plasma particles are usually closed through the quasineutrality condition, $n_e \approx n_i = n$. This condition presumes sufficiently long-wavelength waves, compared to the Debye length. This eliminates the need for Poisson's equation and allows one to unambiguously determine the turbulent total electric field, $\delta \vec{E} = \vec{E} - \vec{E}_0 = -\nabla \delta \Phi$, where $\delta \Phi$ is the corresponding electrostatic potential.

Wave perturbations of the particle temperatures are crucial for the aforementioned thermal instabilities, but for the pure FBI the temperatures T_s can be assumed, e.g., constant, $T_s \approx T_{s0}$ (the isothermal regime) or obeying the adiabatic regime, $T_s \propto n_s^{3/2}$ ($P_s \propto n_s^{5/2}$); the latter is derived by equation (1c) if the right-hand side (RHS) equals zero. Assuming any of these regimes, the fluid-model description of the pure FBI no longer requires equation (1c).

The electron inertia in the corresponding left-hand side (LHS) of equation (1b) never plays a role for low-frequency E-region processes (Dimant & Oppenheim, 2011). For inertialess electrons, equation (1b) yields a simple explicit expression for the electron flow velocity in terms of \vec{E} and ∇P_e :

$$\vec{V}_e \approx -\frac{1}{m_e} \begin{bmatrix} \nu_{en}/\omega_{ec}^2 & 1/\omega_{ec} & 0 \\ -1/\omega_{ec} & \nu_{en}/\omega_{ec}^2 & 0 \\ 0 & 0 & 1/\nu_{en} \end{bmatrix} \times \left[e\vec{E} + \frac{\nabla P_e}{n} \right], \quad (2)$$

where we used the aforementioned condition of $\omega_{ec} \gg \nu_{en}$. The 3-D vector combination $[\vec{A}]$ on the far right of equation (2) implies a right-handed Cartesian coordinate system $[A_x, A_y, A_z]$ with the z -axis directed along \vec{B} . In the preceding 3×3 matrix $[B_{\alpha\beta}]$, the two equal diagonal elements, ν_{en}/ω_{ec}^2 , correspond to the electron Pedersen mobility, the remaining diagonal element, $1/\nu_{en}$, corresponds to the parallel to \vec{B} mobility, whereas the two non-zero non-diagonal elements, $\pm 1/\omega_{ec}$, describe the Hall mobility of the strongly magnetized electrons. Equation (2) applies to both the zero-order background electron flow velocity, \vec{V}_e , and wave perturbations, $\delta\vec{V}_e$. For ions, however, the particle inertia in the LHS of equation (1b) is crucial for driving the FBI. As a result, the expression for the background ion flow velocity, \vec{V}_{i0} , is analogous to equation (2), while the corresponding wave perturbations, $\delta\vec{V}_i$, are described in a more complex way (see, e.g., Dimant & Oppenheim, 2011).

In the E-region ionosphere, strongly magnetized electrons move against the neutral atmosphere with approximately the $\vec{E}_0 \times \vec{B}$ -drift velocity, $\vec{V}_{e0} \approx \vec{V}_0$, while unmagnetized ions are almost attached to the neutral atmosphere. The background charged-particle temperatures are usually larger than the neutral temperature, in part due to the ohmic heating by the driving DC field, \vec{E}_0 . The background parameters determine the phase velocity of the linearly generated waves, the linear growth rate, and the threshold-field amplitude for exciting the FBI, E_{Thr} . The minimum threshold field is usually reached for sufficiently long-wavelength waves, compared to the ion-neutral (i - n) collision mean free path, and for the wavevectors \vec{k} parallel to \vec{V}_0 . Near the optimum wavevector direction in the perpendicular to \vec{B} plane, with small but finite $k_{\parallel} \ll k_{\perp}$, the FBI threshold-field amplitude can be written in the form given, e.g., by Dimant and Milikh (2003); Milikh and Dimant (2003):

$$E_{\text{Thr}} = (1 + \psi) \left(\frac{1 + \kappa_i^2}{1 - \kappa_i^2} \right)^{1/2} E_1, \quad (3)$$

where $\kappa_s = \omega_{sc}/\nu_s$ are the magnetization parameters for the s -species and

$$\psi = \frac{1}{\kappa_e \kappa_i} \left(1 + \frac{k_{\parallel}^2 \omega_{ec}^2}{k_{\perp}^2 \nu_{en}^2} \right). \quad (4)$$

Equation (3) implies $\kappa_i < 1$, since above the ion magnetization boundary, $\kappa_i = 1$, at high latitudes located around 120 km of altitude, the pure FBI cannot be excited, as stated in Dimant and Oppenheim (2004). In the RHS of equation (2), the smallest FBI threshold field, E_1 , corresponding to altitudes with concurrently small ψ and κ_i^2 (Dimant & Oppenheim, 2004, Fig. 5) is given by

$$E_1 = C_s B = 20 \left(\frac{T_e + T_i}{600 \text{ K}} \right)^{1/2} \left(\frac{B}{5 \times 10^4 \text{ nT}} \right) \text{ mV/m}, \quad (5)$$

where $C_s = [(T_e + T_i)/m_i]^{1/2}$ is the isothermal ion-acoustic speed. For the adiabatic regime of instability generation, one must replace T_s with $(5/3)T_s$.

Equations (1)–(5) hold for the particle velocity distributions that are reasonably close to Maxwellian. However, during strong diffuse or discrete aurora, the electron distribution function changes dramatically: in addition to the nearly Maxwellian cold-temperature thermal bulk with energies well below 0.1 eV, a significant superthermal tail develops within the eV-to-tens of keV energy range, as we discuss in more detail in the following sections. With significant non-Maxwellian additions to the velocity distribution, approximate fluid-model equations (1)–(2) lose their validity, as we demonstrate below in section 4. Processes with non-Maxwellian velocity distributions require the kinetic description.

For the kinetic treatment, of significant importance is the fact that after e - n collisions most electrons change their momentum at a much higher rate than they lose their

energy. This means that e - n collisions effectively scatter electrons by large angles in the velocity space with only small relative changes in their kinetic energies. As a result, the electron distribution function remains almost isotropic, $f_e(\vec{V}) \approx F_0(V)$ (here $V \equiv |\vec{V}_e|$), but $F_0(V)$ may deviate significantly from the Maxwellian velocity distribution. Due to this effective isotropization, when calculating integral scalar quantities like the local electron density or pressure, instead of the general 3-D velocity integration one can use a much simpler 1-D speed integration, $\int(\dots)f_0(\vec{V})d^3V \approx 4\pi \int_0^\infty(\dots)F_0(V)V^2dV$.

In particular, the total electron density, pressure, and temperature, used in fluid-model equation (1), become:

$$n_e \approx 4\pi \int_0^\infty F_0(V)V^2dV, \quad (6a)$$

$$P_e = n_e T_{\text{tot}} \approx \frac{4\pi m_e}{3} \int_0^\infty F_0(V)V^4dV, \quad (6b)$$

$$T_{\text{tot}} \approx \frac{4\pi m_e}{3n_0} \int_0^\infty F_0(V)V^4dV = \frac{m_e \int_0^\infty F_0(V)V^4dV}{3 \int_0^\infty F_0(V)V^2dV}. \quad (6c)$$

It is important that the dominant omnidirectional part of the electron distribution function, $F_0(V)$, includes both the thermal bulk and superthermal tail. As we demonstrate below, the relative addition of superthermal particles to the total electron density, n_e , is usually small and can be neglected, $n_e \approx n_0$, while the total temperature, T_{tot} , due to the additional multiplier V^2 in the integrand of (6c), can exceed the electron bulk temperature, T_{e0} , dramatically. Note that in the high-latitude nighttime E-region ionosphere a significant fraction of the thermal bulk plasma may originate from the electron precipitation followed by ionizing collisions of the precipitated energetic electrons. However, this happens only after multiple collisions causing the electrons to have already cooled down and become the effectively ‘maxwellized’ distribution within the cold-temperature thermal bulk. This cold plasma is redistributed by drifts between different locations and can survive without the local precipitation source for a sufficiently long time.

A naive viewpoint suggests using the modified temperature given by equation (6c) to determine the modified FBI threshold by merely replacing in equation (5) the regular electron temperature T_0 with T_{tot} . However, the analysis of section 4 below shows that the velocity dependence of the e - n collision frequency of electrons makes this approach inaccurate.

2.2 Electron Precipitation and STET code

The electron energy distribution in the aurora displays many different forms that are usually described by qualitative criteria developed by Newell et al. (2009, 2010). The majority of these electron distributions are classified as diffuse, monoenergetic, or broadband. Details of these characterization criteria and the origin of different class of electron precipitation phenomena were discussed by McIntosh and Anderson (2014) and will not be repeated here.

The diffuse aurora is primarily caused by wave-particle interactions of high energy electrons, $\mathcal{E} \equiv m_e V^2/2 > 1$ keV, within the plasma sheet (Thorne et al., 2010). Note that since in this paper we treat only electrons kinetically, we will drop subscripts e from any kinetic characteristics (like V).

The non-steady state SuperThermal Electron Transport (STET) code, used in this project, was initially developed by Khazanov et al. (1993) for SE transport in the plasmasphere. Later, this code was further generalized for MI coupling studies in the region of diffuse and monoenergetic auroras by Khazanov et al. (2014); Khazanov, Himwich, et al. (2016); Khazanov, Glocer, et al. (2016); Khazanov et al. (2017); Khazanov, Sibeck, and Chu (2021) and validated experimentally by Samara et al. (2017) in their case study

of a pulsating auroral event imaged optically at high time resolution. The results of our simulation were also successfully compared to FAST (Khazanov, Himwich, et al., 2016; Khazanov, Glocer, et al., 2016) and DMSP (Khazanov, Glocer, & Chu, 2021) observations.

There are different settings available for the application of the STET model for studying the diffuse aurora. The first setting involves imposing a spectrum of primary precipitating electrons with energies above 500–600 eV at an altitude of 800 km and keeping the spectra unchanged (Khazanov, Glocer, et al., 2016). This setting implicitly assumes no MI coupling processes for the energy range of the imposed precipitation and implies the usage of experimental energy fluxes as the boundary conditions. Khazanov, Glocer, et al. (2016) introduced a modification of this boundary condition setting to account for the role of multiple reflections (backscatters) of degraded primary electrons traveling between two magnetically conjugate hemispheres. The latest setting is adapted in the studies that are presented below.

The STET setting in the region of monoenergetic aurora is similar, but assumes the existence of the electrostatic acceleration region located at altitudes of $(1.5-2)R_E$ (Marklund et al., 2011), where R_E is the Earth’s radius. Specifically, STET code was set up to run from the northern or southern hemispheres from 90 km to $2R_E$, where R_E is the Earth’s radius, with the multiple reflection (backscatter) of the electrons whose electrostatic energies are smaller than the potential drop of the acceleration region.

In the analysis presented below, in order to describe the primary magnetosphere-driven electron precipitation in the region of diffuse aurora, we used only the Maxwellian EDF input in the energy range of 600 eV to 30 keV,

$$\Phi(\mathcal{E}) = C\mathcal{E}e^{-\mathcal{E}/\mathcal{E}_0}, \quad (7)$$

where $\Phi = 2\mathcal{E}f_e(\vec{V}, s, t)/m^2$ is the SE flux (Khazanov, 2011), \mathcal{E}_0 is the characteristic energy of plasmasheet electrons, and C is the normalization constant for the selection of the integrated energy flux driven by magnetospheric processes. In the region of monoenergetic aurora, we selected the Gaussian distribution, as in Banks et al. (1974),

$$\Phi(\mathcal{E}) = A \exp[-(\mathcal{E} - \mathcal{E}_0)^2/(2\sigma^2)], \quad \sigma = 0.1\mathcal{E}_0. \quad (8)$$

Here \mathcal{E}_0 is also the characteristic energy of monoenergetic accelerated electrons and A is the normalization constant for the selection of the integrated energy flux as defined above, but only for the electrostatic acceleration region.

In accord with equation (6), the density and pressure of the superthermal electron population, were found using

$$n_{SE} = 4\pi \int_{\mathcal{E}_{\min}}^{\mathcal{E}_{\max}} \frac{\Phi_0}{V(\mathcal{E})} d\mathcal{E}, \quad (9a)$$

$$P_{SE} = \frac{4\pi}{3} \int_{\mathcal{E}_{\min}}^{\mathcal{E}_{\max}} \frac{\mathcal{E}\Phi_0}{V(\mathcal{E})} d\mathcal{E}, \quad (9b)$$

where $V(\mathcal{E}) = (2\mathcal{E}/m_e)^{1/2}$. The minimum and maximum superthermal energies used in our simulations were $\mathcal{E}_{\min} = 1$ eV and $\mathcal{E}_{\max} = 30$ keV, respectively.

These values of n_{SE} and P_{SE} are calculated below for different types of precipitated electron spectra of equations (7) and (8), modeling the diffuse and monoenergetic auroras, respectively. We used the following inputs into the STET model. The neutral thermospheric densities and temperatures were given by MSIS-90 (Hedin, 1991). The electron profile in the ionosphere was calculated based on the IRI model (Bilitza et al., 2017) and extended into the magnetosphere under the assumption that the electron thermal density distribution in the magnetosphere is proportional to the geomagnetic field as $n_e \propto B^{1/2}$. Cross-sections for elastic collisions, state-specific excitation, and ionization were taken from Solomon et al. (1988).

Table 1. Nighttime cold thermal background from the IRI model

Altitude, km	Background density, cm^{-3}	Background pressure, eV cm^{-3}
100	1.67×10^3	53.1
110	2.59×10^3	82.4
120	1.08×10^3	34.2

Table 1a. Maxwellian EDF, $\mathcal{E}_0 = 1$ keV

Altitude, km	A_n , cm^{-3}	A_P , eV cm^{-3}
100	2.06	18.6
110	21	180
120	82	635

3 Results of Kinetic Simulation

Before presenting the simulation results, we notice the following. In our simulations, we neglect any collisions between the superthermal particles themselves, compared to their collisions with the thermal bulk particles. Furthermore, in the lower ionosphere the e - n collisions vastly dominate over Coulomb collisions between the charged particles. With neglect of electron-electron collisions, the corresponding kinetic equation becomes linear with respect to the superthermal particle flux Φ_0 . As a result, given the energy distribution of the precipitated electrons, any superthermal particle-energy-integrated characteristics, such as the density and pressure, will be proportional to the mean energy flux, $\Phi_{\mathcal{E}}$. The latter is defined as the total SE energy (in ergs) per unit square (in cm^2) per unit time (in s) at a given altitude. We will represent the SE density and pressure defined by equation (9) as

$$n_{\text{SE}} = A_n \left(\frac{\Phi_{\mathcal{E}}}{10 \text{ erg cm}^{-2} \text{ s}^{-1}} \right), \quad P_{\text{SE}} = A_P \left(\frac{\Phi_{\mathcal{E}}}{10 \text{ erg cm}^{-2} \text{ s}^{-1}} \right). \quad (10)$$

The characteristic SE density and pressure values, $A_{n,P}$, corresponding to the moderately high energy-flux value of $10 \text{ erg cm}^{-2} \text{ s}^{-1}$, depend on the SE velocity distribution and the ionosphere-thermosphere parameters at given ionospheric altitudes. For our simulations, we picked three E-region altitudes: 100, 110, and 120 km, that best characterize the typical altitude range for the FBI generation.

We performed specific kinetic simulations for the following conditions. Bearing in mind both the discrete and diffuse aurorae, we modeled the Maxwellian EDF given by equation (7) and the Gaussian flux given by equation (8). To characterize various precipitation conditions, we have chosen different values of \mathcal{E}_0 for each EDF (see below). We believe that these values are most characteristic for each kind of storm-time EDF.

To compare the SE contributions to the total electron density and pressure, we have chosen the following values of the nighttime cold thermal background from the IRI model, as shown in Table 1. The background electron temperature for all three altitudes was taken equal, $T_{e0} = 370$ K (corresponding to 0.0318 eV).

Figure 1 shows examples of the corresponding SE velocity distributions. Tables 1a-1c show some simulation results for the Maxwell-input EDF. Tables 2a-2c show some simulation results for the Gaussian EDF.

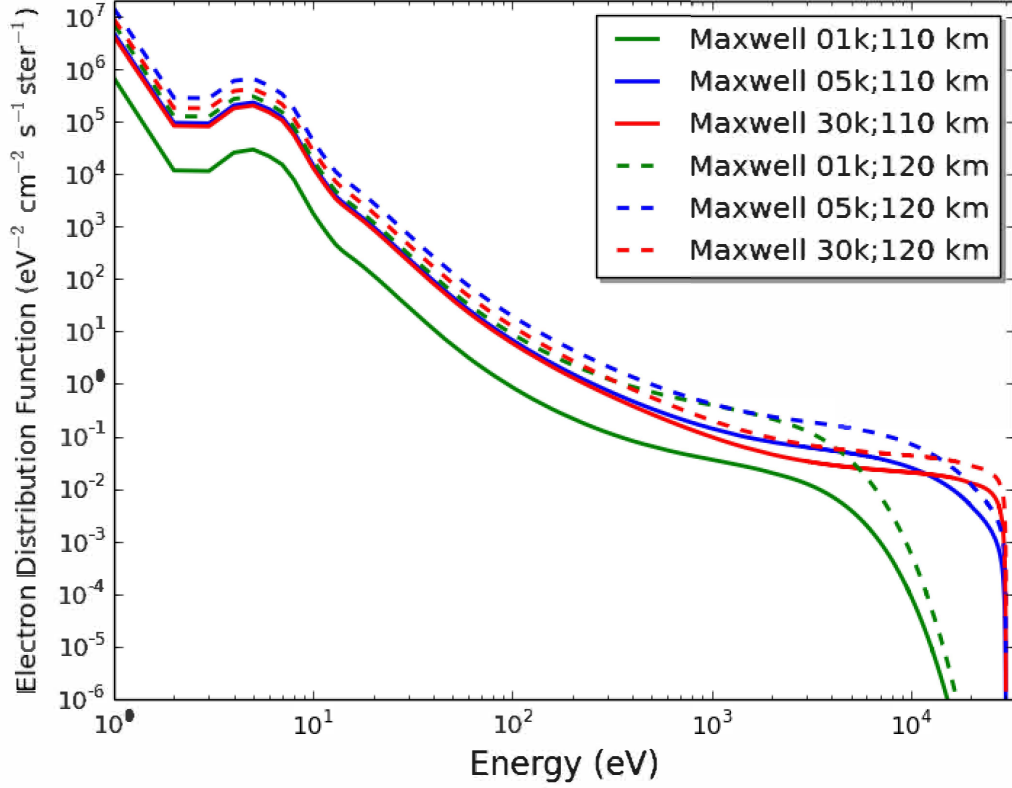


Figure 1. Superthermal electron energy distribution function: some results of kinetic (STET) simulations (Maxwell input); the parameters are shown in the figure.

Table 1b. Maxwellian EDF, $\mathcal{E}_0 = 10$ keV

Altitude, km	A_n , cm^{-3}	A_P , eV cm^{-3}
100	10	604
110	23	1441
120	37	2195

Table 1c. Maxwellian EDF, $\mathcal{E}_0 = 30$ keV

Altitude, km	A_n , cm^{-3}	A_P , eV cm^{-3}
100	13.29	1001
110	28.2	2232
120	41.1	3255

Table 2a. Gaussian EDF, $\mathcal{E}_0 = 1$ keV

Altitude, km	A_n , cm^{-3}	A_P , eV cm^{-3}
100	0.07	4.81×10^{-2}
110	4.45	3.16
120	55.0	41.6

Table 2b. Gaussian EDF, $\mathcal{E}_0 = 10$ keV

Altitude, km	A_n , cm^{-3}	A_P , eV cm^{-3}
100	6.72	158.8
110	18.56	586.4
120	28.41	1047

Table 2c. Gaussian EDF, $\mathcal{E}_0 = 30$ keV

Altitude, km	A_n , cm^{-3}	A_P , eV cm^{-3}
100	6.94	1066
110	12.37	2099
120	15.98	2823

Using the table values along with equation (10) and comparing the simulation results with the typical background parameters, we see that the contribution of the SE tail, n_{SE} , to the total electron density, $n_{\text{tot}} = n_{e0} + n_{\text{SE}}$, is usually small compared to the background density, n_{e0} . For reasonable values of the mean energy flux, $\Phi_{\mathcal{E}} \lesssim 10 \text{ erg cm}^{-2} \text{ s}^{-1}$, even for the large values of \mathcal{E}_0 , the SE contribution to n_{tot} can be neglected.

An entirely different situation, however, takes place for the total pressure, P_{tot} , and hence for the total electron temperature, $P_{\text{tot}} = P_{e0} + P_{\text{SE}}$. Only for the Maxwellian EDF with the smallest calculated SE energy $\mathcal{E}_0 = 1$ keV the SE contributions is comparable to the background values of the electron pressure and temperature; for all other values of \mathcal{E}_0 , $\Phi_{\mathcal{E}} \gtrsim 10 \text{ erg cm}^{-2} \text{ s}^{-1}$, and both kinds of the EDF the SE contributions are much larger than the corresponding background values.

4 Effect of Superthermal Electrons on the FBI Threshold: analytical treatment

As we have already mentioned, the naive calculation of the modified instability threshold based on replacing the undisturbed electron cold-plasma temperature T_e with the modified temperature T_{tot} defined by equation (6) turns out to be incorrect. This will become clear after we implement in section 4.1 a tentative three-fluid approach based on two distinct Maxwellian velocity distributions of electrons (the cold thermal bulk and the energetic tail of precipitated electrons) with two different e - n collision frequencies.

At the E-region altitudes, however, the energy distribution of precipitating electrons deviates significantly from a Maxwellian distribution. Also, the e - n collision frequency depends smoothly on the electron energy and hence cannot be reduced to only

two constant values. All this requires the proper description of the electron behavior to be kinetic. At the same time, for sufficiently long-wavelength and low-frequency waves, as specified below by equation (41), the ion behavior can be successfully described by the much simpler fluid model.

For the kinetic treatment of electrons, we will mostly follow the approximate kinetic approach developed in Dimant and Sudan (1995a). This approach is based on the assumption that e - n collisions lead to much faster angular scatter of electrons in the velocity space than to losses of their energies, as we already mentioned in section 2.1. For superthermal electrons with energies $\mathcal{E} \gtrsim 1$ keV, the two rates are comparable, but the approximate approach of Dimant and Sudan (1995a) is still useful and will lead to reasonably accurate analytic results.

4.1 Three-Fluid Linear Analysis of the FBI

In this section, we outline the simplified 3-fluid model approach by assuming two electron fluids and a single ion one. This oversimplified approach does not rival the rigorous kinetic approach implemented in the following section 4.2, but it will provide useful insight into the effect of electron precipitation on the FBI threshold conditions and will help identify the key factors.

The closed set of fluid-model equations (1) is only valid for the particle velocity distributions reasonably close to Maxwellian, so that in this tentative approach we will use the model of two Maxwellian populations of electrons, $f_e = f_{\text{TB}} + f_{\text{SE}}$, where TB stands for the thermal bulk and SE stands for the superthermal electron tail. Each Maxwellian population has its own density and temperature: $f_{\text{TB}} = n_{\text{TB}} [m_e / (2\pi T_{\text{TB}})]^{3/2} \exp(-\mathcal{E}/T_{\text{TB}})$, and $f_{\text{SE}} = n_{\text{SE}} [m_e / (2\pi T_{\text{SE}})]^{3/2} \exp(-\mathcal{E}/T_{\text{SE}})$. Under the actual conditions of electron precipitation, the conditions $T_{\text{SE}} \gg T_{\text{TB}}$, n_{SE} , and n_{TB} usually hold, although for this specific treatment these conditions are of no importance and will not be imposed.

Adding to the two electron fluids an ion fluid and assuming for simplicity the isothermal regime of the pure FBI with constant T_{TB} , T_{SE} , and T_i but variable densities, n_{SE} , $n_{\text{TB}} \approx n_i$, we will need only two first fluid-model equations (1a) and (1b),

$$\frac{\partial n_j}{\partial t} + \nabla \cdot (n_j \vec{V}_j) = 0, \quad (11a)$$

$$m_j \left(\frac{\partial}{\partial t} + \vec{V}_j \cdot \nabla \right) \vec{V}_j = q_j (\vec{E} + \vec{V}_j \times \vec{B}) - T_j \frac{\nabla n_j}{n_j} - m_j \nu_j \vec{V}_j, \quad (11b)$$

where the subscript j denotes either each of the two electron species, $j = \text{TB}$ and $j = \text{SE}$, or the single ion species, $j = i$. The kinetic e - n collision frequency ν_e depends strongly on the individual electron velocity. To mimic this in our oversimplified three-fluid model, we will assign for each electron population its own constant value of ν_e : the mean thermal bulk value, ν_{TB} , and the mean superthermal value, ν_{SE} . These values of ν_e may be vastly different.

Bearing in mind the long-wavelength and low-frequency E-region processes, we will close all three sets of fluid equations by the quasineutrality condition, $n_i = n_{\text{TB}} + n_{\text{SE}}$, for both the undisturbed plasma background, $n_i^{(0)} = n_{\text{TB}}^{(0)} + n_{\text{SE}}^{(0)}$, and linear wave perturbations, $\delta n_i = \delta n_{\text{TB}} + \delta n_{\text{SE}}$. In what follows, we will mostly operate with the relative fractions of each background electron population, $\rho_{\text{TB}} = n_{\text{TB}}^{(0)} / n_i^{(0)}$ and $\rho_{\text{SE}} = n_{\text{SE}}^{(0)} / n_i^{(0)}$, so that $\rho_{\text{TB}} + \rho_{\text{SE}} = 1$.

For the undisturbed background flows, after setting $\partial/\partial t \rightarrow 0$, $\nabla \rightarrow 0$, equation (1b) yields

$$\vec{V}_{j0} = \left(\frac{q_j \vec{E}_0}{m_j \nu_j} + \kappa_j^2 \vec{V}_0 \right) / (1 + \kappa_j^2), \quad (12)$$

where the $\vec{E}_0 \times \vec{B}$ -drift velocity \vec{V}_0 and magnetization parameters $\kappa_j = \omega_{ce}/\nu_j$ were defined in section 2.1; $q_i = e$, $q_{\text{TB}} = q_{\text{SE}} = -e$; and $m_{\text{TB}} = m_{\text{SE}} = m_e$. In spite of the common value of the electron gyrofrequency ω_{ce} , each Maxwellian electron population, TB and SE, has different magnetization parameters κ_j , $\kappa_{\text{TB}} = \omega_{ce}/\nu_{\text{TB}} \neq \kappa_{\text{SE}} = \omega_{ce}/\nu_{\text{SE}}$. In what follows, we will assume both electron fluids to be strongly magnetized, $\kappa_{\text{TB}}, \kappa_{\text{SE}} \gg 1$, so that the average background flow of all electrons is close to the $\vec{E}_0 \times \vec{B}$ -drift velocity, $\vec{V}_{\text{TB}0} \approx \vec{V}_{\text{SE}0} \approx \vec{V}_0$. For the following analysis, it is also convenient to introduce the velocity difference between the background electron and ion flows:

$$\vec{U} \approx \vec{V}_0 - \vec{V}_{i0} = \left(\vec{V}_0 - \frac{q_i \vec{E}_0}{m_i \nu_i} \right) / (1 + \kappa_i^2). \quad (13)$$

In all low-frequency E-region processes, electric fields are electrostatic, $\vec{E} = -\nabla\Phi$, while the magnetic field \vec{B} remains essentially constant. For linear wave perturbations of all space/time-varying quantities, we will set the standard harmonic-wave ansatz: $\delta A \propto \exp[i(\vec{k} \cdot \vec{r} - \omega t)]$ with real \vec{k} , but complex frequency, $\omega = \omega_r + i\gamma$.

Introducing dimensionless variables for each species j :

$$\eta_j \equiv \frac{\delta n_j}{n_{j0}}, \quad \phi \equiv \frac{e\delta\Phi}{T_{i0}}, \quad (14)$$

we obtain from continuity equation (1a) a simple relation:

$$\eta_j = \frac{\vec{k} \cdot \delta \vec{V}_j}{\Omega_j}, \quad (15)$$

where $\Omega_j \equiv \omega - \vec{k} \cdot \vec{V}_{j0}$ is the Doppler-shifted wave frequency in the frame of reference of the j -species mean flow. The j -fluid velocity perturbation $\delta \vec{V}_j$ should be found from momentum-balance equation (1b). In the dimensionless variables, all $\delta \vec{V}_j$ become proportional to the normalized linear combinations of the linearized wave electric field with the particle pressure perturbations, $\alpha_j \phi + \eta_j$, where

$$\alpha_i = 1, \quad \alpha_{\text{TB}} = -\frac{T_{i0}}{T_{\text{TB}}}, \quad \alpha_{\text{SE}} = -\frac{T_{i0}}{T_{\text{SE}}}. \quad (16)$$

Then equation (15) yields η_j in terms of ϕ ,

$$\eta_j = \frac{\alpha_j A_j}{1 - A_j} \phi, \quad A_j \equiv \frac{\vec{k} \cdot \delta \vec{V}_j}{(\alpha_j \phi + \eta_j) \Omega_j}, \quad (17)$$

via still undetermined coefficients A_j . In the direction parallel to \vec{B} , equation (1b) yields

$$\delta \vec{V}_{j\parallel} = -i \frac{\vec{k}_{\parallel} V_{Tj}^2 (\alpha_j \phi + \eta_j)}{\nu_j (1 - i\Omega_j/\nu_j)}, \quad (18)$$

while in the perpendicular to \vec{B} component of $\delta \vec{V}_j$, we have a more complicated relation,

$$\delta \vec{V}_{j\perp} = -i \frac{V_{Tj}^2}{\nu_j} \frac{(1 - i\Omega_j/\nu_j) \vec{k}_{\perp} + \kappa_j (\vec{k}_{\perp} \times \hat{b})}{(1 - i\Omega_j/\nu_j)^2 + \kappa_j^2} (\alpha_j \phi + \eta_j), \quad (19)$$

where \vec{k}_{\parallel} and \vec{k}_{\perp} are the wavevector components in the parallel and perpendicular to \vec{B} directions, respectively. For the coefficients A_j , these equations yield

$$A_j = -i \frac{V_{Tj}^2}{\nu_j \Omega_j} \left[\frac{(1 - i\Omega_j/\nu_j) k_{\perp}^2}{(1 - i\Omega_j/\nu_j)^2 + \kappa_j^2} + \frac{k_{\parallel}^2}{1 - i\Omega_j/\nu_j} \right]. \quad (20)$$

Using the quasineutrality condition for the wave perturbations, $\eta_i = \rho_{\text{TB}}\eta_{\text{TB}} + \rho_{\text{SE}}\eta_{\text{SE}}$, we obtain from equations (17) and (20) the three-fluid FBI dispersion relation:

$$D(\omega, \vec{k}) \equiv 1 + \frac{1 - A_i}{A_i} \left(\frac{\rho_{\text{TB}}|\alpha_{\text{TB}}|A_{\text{TB}}}{1 - A_{\text{TB}}} + \frac{\rho_{\text{SE}}|\alpha_{\text{SE}}|A_{\text{SE}}}{1 - A_{\text{SE}}} \right) = 0, \quad (21)$$

where we have used the fact that both α_{TB} and α_{SE} are negative, as seen from equation (16).

General three-fluid FBI dispersion relation, equation (21), does not have a simple general solution. Fortunately, it can be simplified by taking into account the fact that fluid-model equation (1) is valid only in the long-wavelength limit in which all wave vectors are much larger than the corresponding ion collisional mean free paths, while the wave frequencies are small compared to the ion-neutral collision frequencies, $|\omega|, kV_{i0}, kV_{Ti} \ll \nu_i$. Otherwise, ion Landau damping becomes crucial, requiring the kinetic treatment of ions. It is also important that the minimum values of the FBI threshold field are always reached in the same long-wavelength limit, where we automatically obtain $|A_j| \ll 1$. Assuming also $|\Omega_{\text{TB}}/\nu_{\text{TB}}|, |\Omega_{\text{SE}}/\nu_{\text{SE}}| \ll |\Omega_i/\nu_i|, k_{\parallel}^2 \ll k_{\perp}^2$, and $\kappa_i \lesssim 1$, we obtain for all A_j simpler expressions:

$$A_{\text{TB}} \approx -i \frac{k_{\perp}^2 V_{T\text{TB}}^2 (1 + \kappa_{\text{TB}}^2 k_{\parallel}^2 / k_{\perp}^2)}{\nu_{\text{TB}} \Omega_{\text{TB}} \kappa_{\text{TB}}^2 (1 - i\Omega_{\text{TB}}/\nu_{\text{TB}})}, \quad (22a)$$

$$A_{\text{SE}} \approx -i \frac{k_{\perp}^2 V_{T\text{SE}}^2 (1 + \kappa_{\text{SE}}^2 k_{\parallel}^2 / k_{\perp}^2)}{\nu_{\text{SE}} \Omega_{\text{SE}} \kappa_{\text{SE}}^2 (1 - i\Omega_{\text{SE}}/\nu_{\text{SE}})}, \quad (22b)$$

$$A_i \approx -i \frac{k_{\perp}^2 V_{Ti}^2 (1 - i\Omega_i/\nu_i)}{\nu_i \Omega_i [(1 - i\Omega_i/\nu_i)^2 + \kappa_i^2]}. \quad (22c)$$

Then, to the first-order accuracy with respect to small $|A_j|$, general three-fluid FBI dispersion equation (21) reduces to

$$D(\omega, \vec{k}) \approx 1 + \frac{\rho_{\text{TB}}|\alpha_{\text{TB}}|A_{\text{TB}}}{A_i} (1 + A_{\text{TB}} - A_i) + \frac{\rho_{\text{SE}}|\alpha_{\text{SE}}|A_{\text{SE}}}{A_i} (1 + A_{\text{SE}} - A_i) = 0. \quad (23)$$

This reduced dispersion relation has certain advantages over general equation (21). First, in the assumed long-wavelength limit, $|\text{Im} D(\omega, \vec{k})|$ turns out to be automatically small compared to $|\text{Re} D(\omega, \vec{k})|$, as well as the growth/damping rate, $|\gamma|$, becomes small compared to the real wave frequency, ω_r . This allows one to treat the wave phase-velocity relation derived by the dominant real part of $D(\omega, \vec{k})$, separately from the instability driving derived by the small imaginary part of $D(\omega, \vec{k})$. Second, equation (23) allows one to expose all instability driving and loss mechanisms as separate linear terms. This is convenient for the general instability analysis, although here we restrict ourselves to the purely isothermal FBI.

Under condition of $|\gamma| \ll \omega_r$, if we also neglect the corresponding first-order small terms in the RHS of equation (23) and substitute $\omega \approx \omega_r$ in all highest-order terms, we obtain the equation for the real wave frequency, $\text{Re} D(\omega, \vec{k}) \approx D_0(\omega_r, \vec{k})$. The solution of $D_0(\omega_r, \vec{k}) = 0$ for $\text{Re} \omega = \omega_r$ provides the zeroth-order phase-velocity relations for the linear harmonic waves, $\omega_r(\vec{k})$. In the next step, we add the small imaginary parts and solve for the first-order equation with $i\gamma$ included in the complex wave frequency. This gives

$$\gamma \approx - \left. \frac{\text{Im} D(\omega, \vec{k})}{\partial D_0(\omega, \vec{k}) / \partial \omega} \right|_{\omega=\omega_r}. \quad (24)$$

The zeroth-order relation for the dominant real part of the wave frequency is obtained by neglecting in the RHS of equation (23) all terms proportional to A_j , except

the ratios A_{TB}/A_i and A_{SE}/A_i . This yields

$$D_0(\omega_r, \vec{k}) = 1 + (1 + \kappa_i^2) \left(1 + \frac{\vec{k} \cdot \vec{U}}{\Omega_e} \right) \Psi = 0, \quad (25)$$

where Ω_e is the common Doppler-shifted wave frequency for all electrons, $\Omega_e = \Omega_{\text{TB}} = \Omega_{\text{SE}} \approx \omega_r - \vec{k} \cdot \vec{V}_0$,

$$\Psi \equiv \rho_{\text{TB}} \psi_{\text{TB}} + \rho_{\text{SE}} \psi_{\text{SE}}, \quad \psi_j \equiv \frac{1}{\kappa_j \kappa_i} \left(1 + \frac{\kappa_j^2 k_{\parallel}^2}{k_{\perp}^2} \right), \quad (26)$$

and \vec{U} is defined by equation (13) with the use of the relation $\Omega_i = \Omega_e + \vec{k} \cdot \vec{U}$. The solution of equation (25) for Ω_e yields

$$\begin{aligned} \Omega_e(\vec{k}) &= - \frac{(1 + \kappa_i^2)(\vec{k} \cdot \vec{U}) \Psi}{1 + (1 + \kappa_i^2) \Psi}, \\ \Omega_i(\vec{k}) &= \frac{\vec{k} \cdot \vec{U}}{1 + (1 + \kappa_i^2) \Psi}, \\ \omega_r(\vec{k}) &= \frac{\vec{k} \cdot [\vec{V}_0 + (1 + \kappa_i^2) \Psi \vec{V}_{i0}]}{1 + (1 + \kappa_i^2) \Psi}. \end{aligned} \quad (27)$$

These expressions provide the phase-velocity relation, $\vec{V}_{\text{ph}} = \omega_r(\vec{k})/\vec{k}$, in various frames of reference. For the low ion magnetization, $\kappa_i^2 \ll 1$, $|\vec{V}_{i0}| \ll V_0$, $\vec{U}_i \approx \vec{V}_0$, that usually takes place at E-region altitudes below 115 km, we have much simpler relations:

$$\Omega_e \approx - \frac{\Psi(\vec{k} \cdot \vec{V}_0)}{1 + \Psi}, \quad \Omega_i \approx \omega_r \approx \frac{\vec{k} \cdot \vec{V}_0}{1 + \Psi}. \quad (28)$$

They become the conventional FBI expressions if the parameter Ψ defined in equation (26) is replaced by the single-group parameter $\psi_e = (\nu_e \nu_i / \omega_{ce} \omega_{ci})(1 + \omega_{ce}^2 k_{\parallel}^2 / \nu_e^2 k_{\perp}^2)$. Note also that in the long-wavelength limit the phase-velocity relations given by (27)–(28) are common for all E-region instabilities.

Calculating the FBI growth rate requires more cumbersome algebra. Skipping most of it, we obtain

$$\begin{aligned} \text{Im } D(\omega, \vec{k}) &= \frac{1}{\nu_i \Omega_i} \left\{ \Omega_i^2 - \left[1 + \frac{\rho_{\text{TB}} \psi_{\text{TB}}^2 T_{\text{TB}} + \rho_{\text{SE}} \psi_{\text{SE}}^2 T_{\text{SE}}}{\Psi^2 T_i} \right] k_{\perp}^2 V_{Ti}^2 \right\}, \\ \frac{\partial D_0(\omega_r, \vec{k})}{\partial \omega_r} &= - \frac{1}{\Psi(\vec{k} \cdot \vec{U}_i)}, \end{aligned}$$

where Ω_i is given by equation (27) and $V_{Ti}^2 = T_i/m_i$. Then equation (24) yields

$$\begin{aligned} \gamma &= \frac{\Psi}{[1 + (1 + \kappa_i^2) \Psi] \nu_i} \left\{ \left[1 - \kappa_i^2 - \frac{(1 + \kappa_i^2)^2 \nu_i^2}{\omega_{pi}^2} \right] \Omega_i^2 \right. \\ &\quad \left. - \left(1 + \frac{\rho_{\text{TB}} \psi_{\text{TB}}^2 T_{\text{TB}} + \rho_{\text{SE}} \psi_{\text{SE}}^2 T_{\text{SE}}}{\Psi^2 T_i} \right) k_{\perp}^2 V_{Ti}^2 \right\}, \end{aligned} \quad (29)$$

where $\omega_{pi} = [n_0 e^2 / (\epsilon_0 m_i)]^{1/2}$ is the ion plasma frequency. Equating $\gamma = 0$, we obtain the expression for $\Omega_i(\vec{k})$ and, through equations (13) and (27), the threshold values of the FBI driving field, $E_{\text{Thr}}(\vec{k})$.

We will not analyze here expression (29) because the three-fluid model is too oversimplified and cannot provide accurate quantitative description of the FBI in the presence of the electron precipitation. The main point of this tentative analysis was to demonstrate the unexpected complexity of the parameter dependence. The contribution of the

partial parameters ψ_{TB} and ψ_{SE} into the total parameter Ψ , as described by equation (26), is natural and well-expected generalization. What was not expected though is the explicit involvement of these partial parameters into the weighting factors for T_{TB} and T_{SE} within the FBI diffusion loss term $\propto k_{\perp}^2 V_{Ti}^2$. If there were no additional weighting factors ψ_{TB}^2 and ψ_{SE}^2 then the three-fluid model expression for the growth/damping rate γ would correspond to the naively suggested replacement of the electron temperature with the effective temperature T_{tot} defined by equation (6c). However, the additional multipliers ψ_{TB}^2 and ψ_{SE}^2 , each proportional to ν_{TB}^2 and ν_{SE}^2 , respectively, makes the contribution of each electron group into the FBI loss term much less obvious with potentially significant quantitative consequences.

Since the e - n collision frequency has a gradual dependence on the individual electron velocity, this dependence cannot be accurately reduced to just two different constant values ν_{TB} and ν_{SE} , as we have done in this tentative analysis. The only proper and accurate way to quantitatively treat electron collisions for the two-component electron distribution with non-Maxwellian high-energy tail is by employing the rigorous kinetic theory. This will be done in the following section.

4.2 Kinetic Analysis of the FBI Onset for the General Electron Distribution Function

In this section, we develop a kinetic linear theory of the FBI for a system with general non-Maxwellian electron distributions. Our hybrid theoretical approach combines the fully kinetic description of electrons with the fluid-model description of ions.

As above, we will restrict our treatment to the E-region altitudes where the electrons are highly magnetized, $\omega_{ec} \gg \nu_{en}$, while ions are at least partially unmagnetized, $\omega_{ic} \lesssim \nu_{in}$. These conditions typically hold within the core of the high-latitude E-region ionosphere between 90 and 120 km. Under these magnetization conditions, electrons are essentially $\vec{E}_0 \times \vec{B}$ drift, while ions mostly move with the dominant neutral component. The linear instability onset is described by analyzing small harmonic wave perturbations of the plasma particle motion and the coupled electrostatic potential.

Before proceeding with the fluid-model ion description, we introduce dimensionless variables and parameters:

$$\eta_{\omega, \vec{k}} \equiv \frac{\delta n_{\omega, \vec{k}}}{n_0}, \quad \phi_{\omega, \vec{k}} \equiv \frac{e\Phi_{\omega, \vec{k}}}{T_{e0}}, \quad \beta_T \equiv \frac{T_{i0}}{T_{e0}}, \quad (30)$$

where T_{e0} is an effective electron temperature, while the entire ion population is assumed to be Maxwellian with the constant temperature T_{i0} . For the general non-Maxwellian electron distribution, we will not specify the parameter T_{e0} . We have introduced it here as a convenient normalization constant, but the final expressions will not depend on T_{e0} .

For isothermal ions, the fluid model equations (1a) and (1b) yield the following relation between $\phi_{\omega, \vec{k}}$ and $\eta_{\omega, \vec{k}}$:

$$\phi_{\omega, \vec{k}} \approx \beta_T \left\{ \left[\frac{(1 - \kappa_i^2) \Omega_{\omega, k} + i(1 + \kappa_i^2) \nu_{in}}{k^2 V_{Ti}^2} \Omega_{\omega, \vec{k}} - 1 \right] \eta_{\omega, \vec{k}}, \right. \quad (31)$$

where $\Omega_{\omega, \vec{k}} \equiv \omega - \vec{k} \cdot \vec{V}_{i0}$ is the Doppler-shifted wave frequency in the ion-flow frame of reference, moving relative the neutrals with the mean flow velocity,

$$\vec{V}_{i0} = \left(\frac{e\vec{E}_0}{m_i \nu_{in}} + \kappa_i^2 \vec{V}_0 \right) / (1 + \kappa_i^2), \quad (32)$$

and $V_{Ti} = (T_{i0}/m_i)^{1/2}$ is the ion thermal velocity. Recall that $\vec{V}_0 = \vec{E}_0 \times \vec{B}/B^2$ is the $\vec{E}_0 \times \vec{B}$ -drift velocity and $\kappa_i = \omega_{ic}/\nu_{in}$ is the ion magnetization parameter. The

full expression for \vec{V}_{i0} is of importance only for altitudes above 115 km where $\kappa_i \gtrsim 1$. At altitudes well below 115 km, the ions are essentially unmagnetized, $\kappa_i \ll 1$, $\nu_{in} \gg \omega_{ic}$, so that the mean ion-flow speed is negligibly small compared the mean speed of the highly magnetized electrons $V_0 = |\vec{V}_0| = eE_0/(m_i\omega_{ic})$.

Here we generalize the kinetic description of electrons in Dimant and Sudan (1995a) by assuming arbitrary ion magnetization and, more importantly, by assuming non-Maxwellian velocity distribution of the background electrons.

If we suppose that collisional angular scattering of electrons is much faster than the corresponding energy changes then the electron velocity distribution consists mostly of two different parts,

$$f_e(\vec{V}, \vec{r}) \approx F_0(V, \vec{r}) + \frac{\vec{f}_1(V, \vec{r}) \cdot \vec{V}}{V}, \quad |\vec{f}_1(V, \vec{r})| \ll F_0(V, \vec{r}), \quad (33)$$

where \vec{V} is the electron velocity and V is the corresponding speed. The function $F_0(V, \vec{r})$ is the dominant omnidirectional, i.e., isotropic, part of $f_e(\vec{V}, \vec{r})$, while $\vec{f}_1(V, \vec{r})$ is a small directional part. The isotropic part $F_0(V, \vec{r})$ is responsible for the integral scalar quantities like the total electron density, pressure,

$$n_e(\vec{r}) \approx 4\pi \int_0^\infty F_0(V, \vec{r}) V^2 dV, \quad P_e(\vec{r}) \approx \frac{4\pi m_e}{3} \int_0^\infty F_0(V, \vec{r}) V^4 dV, \quad (34)$$

and temperature, $T_{\text{tot}}(\vec{r}) = P_e(\vec{r})/n_e(\vec{r})$, while the small directional part is responsible for various fluxes and currents, like the total particle number flux,

$$\vec{\Gamma}(\vec{r}) \approx \frac{4\pi}{3} \int_0^\infty \vec{f}_1(V, \vec{r}) V^3 dV \quad (35)$$

and the corresponding energy flux. Equation (33) represents the two highest-order terms of the Legendre polynomial series (Shkarofsky et al., 1966; Gurevich, 1978; Khazanov, 2011). No higher-order angular dependencies of $f_e(\vec{V}, \vec{r})$, responsible for the anisotropic pressure, viscosity tensors, etc., are included in approximate equation (33).

Under conditions of strong isotropization of the electron distribution function, the general kinetic equation reduces to a set of two coupled integro-differential equations (Dimant & Sudan, 1995a, equations (11) and (12)), whose further simplification results in $\vec{f}_1(V, \vec{r})$ explicitly expressed in terms of $F_0(V, \vec{r})$ (Dimant & Sudan, 1995a, equations (13) and (14)). This allows one to obtain a closed partial differential equation for $F_0(V, \vec{r})$,

$$\left(\frac{\partial}{\partial t} + \vec{V}_{\text{dr}} \cdot \nabla + \hat{R} \right) F_0(V, \vec{r}) = 0, \quad (36)$$

where the total $\vec{E} \times \vec{B}$ -drift velocity is given by

$$\vec{V}_{\text{dr}} \equiv \vec{V}_0 + \frac{e}{m_e \omega_{ec}} \hat{b} \times \nabla \Phi, \quad (37)$$

and the differential operator \hat{R} is given by

$$\begin{aligned} \hat{R} &\equiv -\frac{1}{3V^2} \left(\hat{\mathbf{K}}_\perp \cdot \frac{V^2 \nu_{en}(V)}{\omega_{ec}^2} \hat{\mathbf{K}}_\perp + \hat{K}_\parallel \frac{V^2}{\nu_{en}(V)} \hat{K}_\parallel \right), \\ \hat{\mathbf{K}}_\perp &\equiv V \nabla_\perp - \frac{e \vec{E}_\perp}{m_e} \frac{\partial}{\partial V}, \quad \hat{K}_\parallel \equiv V \frac{\partial}{\partial z} - \frac{e E_\parallel}{m_e} \frac{\partial}{\partial V}, \end{aligned} \quad (38)$$

where $\partial/\partial z$ is the derivative in the \vec{B} direction; E_\parallel and \vec{E}_\perp are the parallel and perpendicular to \vec{B} components of the total electrostatic field, $\vec{E} = \vec{E}_0 - \nabla \Phi$; and $\hat{b} = \vec{B}/b$ is the unit vector in the \vec{B} direction. Equations (36)–(38) differ from Dimant and Sudan (1995a, equations (16)–(23)) by some notations and, most importantly, by neglecting here

the e - e collisions and the terms describing the thermal exchange between electrons and neutrals through e - n collisions. The former is important for sufficiently dense and low-energy particles, while the latter is crucial for the electron thermal instability (ETI) (Dimant & Sudan, 1995b, 1995c, 1997; M. Oppenheim et al., 2020, and references therein). Bearing in mind the pure FBI, we disregard here any thermal-instability effects.

Equation (36) holds for the entire isotropic part of the electron distribution function, $F_0(V, \vec{r})$, which includes the spatially homogeneous background distribution, $f_0(V)$, and all linear wave perturbations, $f_{\omega, \vec{k}}(V)$. Linearizing this equation for a given wave harmonic, after some algebra we arrive at equation (38) from Dimant and Sudan (1995a):

$$\left(i\Delta_{\omega, \vec{k}} + \hat{D}_{\omega, \vec{k}}\right) f_{\omega, \vec{k}}(V) = \left(\hat{B}_{\omega, \vec{k}} F_0(V)\right) \phi_{\omega, \vec{k}}, \quad (39)$$

where various differential operators acting on both $f_{\omega, \vec{k}}$ and F_0 are defined by

$$\hat{D}_{\omega, \vec{k}} \equiv -\frac{1}{3V^2} \left(\hat{\mathbf{K}}_{\perp}^{(0)} \cdot \frac{V^2 \nu_{en}(V)}{\omega_{ec}^2} \hat{\mathbf{K}}_{\perp}^{(0)} + \hat{K}_{\parallel}^{(0)} \frac{V^2}{\nu_{en}(V)} \hat{K}_{\parallel}^{(0)} \right) \quad (40a)$$

$$\Delta_{\omega, \vec{k}} \equiv \vec{k} \cdot \vec{V}_0 - \omega, \quad \hat{\mathbf{K}}_{\perp}^{(0)} = i\vec{k}_{\perp} V - \frac{e\vec{E}_0}{m_e} \frac{d}{dV}, \quad \hat{K}_{\parallel}^{(0)} = ik_{\parallel} V, \quad (40b)$$

$$\begin{aligned} \hat{B}_{\omega, \vec{k}} \equiv & -\frac{T_{e0}}{3m_e} \left[\left(\frac{k_{\perp}^2 \nu_{en}(V)}{\omega_{ec}^2} + \frac{k_{\parallel}^2}{\nu_{en}(V)} \right) V \frac{d}{dV} \right. \\ & \left. + 2i \frac{e\vec{k}_{\perp} \cdot \vec{E}_0}{m_e \omega_{ec}^2 V^2} \frac{d}{dV} \left(V^2 \nu_{en}(V) \frac{d}{dV} \right) \right]. \end{aligned} \quad (40c)$$

Equation (39) implies an arbitrary background distribution function $F_0(V)$ that provides convergence of any integrals, like those in equation (34). In our case, $F_0(V)$ includes both the low-energy Maxwellian bulk distribution and the high-energy superthermal tail, We will specify these components later, but now will proceed with arbitrary $F_0(V)$. Note that the definition $\hat{B}_{\omega, \vec{k}}$ includes the normalization constant T_{e0} in the numerator, while the wave potential $\phi_{\omega, \vec{k}}$, defined in equation (30), contains T_{e0} in the denominator, so that the RHS of (39) is actually T_{e0} -independent.

In accord with the above discussion, we drop all terms proportional to $\vec{k}_{\perp} \cdot \vec{E}_0$ because these terms describe frictional heating and will eventually lead to the ETI. The pure FBI is described by the remaining terms, like the first term in the RHS of equation (40c), which is proportional to Vd/dV .

Now we obtain the second relation between $\eta_{\omega, \vec{k}}$ and $\phi_{\omega, \vec{k}}$, analogous to equation (31). Before proceeding, we specify the main conditions for the vast majority of the FBI-driven waves. These low-frequency and long-wavelength waves usually satisfy

$$k_{\parallel} \ll k_{\perp} \approx k, \quad \gamma \ll \omega, \quad kV_0 \ll \nu_{in}, \quad k\lambda_D \ll 1, \quad (41)$$

so that the following inequality holds,

$$|\hat{D}_{\omega, \vec{k}}| \ll |\Delta_{\omega, \vec{k}}|. \quad (42)$$

These symbolic relation means that the operators $\hat{D}_{\omega, \vec{k}}$ and $\Delta_{\omega, \vec{k}}$ apply to $f_{\omega, \vec{k}}(V)$ and the results are compared by the absolute value. The main point of equation (42) is that one can apply to equation (39) a formal Taylor expansion with respect to the small ratio $|\hat{D}_{\omega, \vec{k}}|/|\Delta_{\omega, \vec{k}}|$. This leads to

$$f_{\omega, \vec{k}}(V) \approx \left(\frac{\hat{B}_{\omega, \vec{k}} F_0(V)}{i\Delta_{\omega, \vec{k}}} + \frac{\hat{D}_{\omega, \vec{k}} \hat{B}_{\omega, \vec{k}} F_0(V)}{\Delta_{\omega, \vec{k}}^2} \right) \phi_{\omega, \vec{k}}, \quad (43)$$

where the order of the two differential operators $\hat{D}_{\omega, \vec{k}}$ and $\hat{B}_{\omega, \vec{k}}$ matters. This formal expansion procedure is equivalent to a regular perturbation technique when one initially

neglects in equation (39) the term $\propto \hat{D}_{\omega, \vec{k}}$ and then finds the first-order correction. Proceeding from $f_{\omega, \vec{k}}$ to $\eta_{\omega, \vec{k}}$ through the relation

$$\eta_{\omega, \vec{k}} = \frac{4\pi \int_0^\infty f_{\omega, \vec{k}}(V) V^2 dV}{n_0} = \frac{\int_0^\infty f_{\omega, \vec{k}}(V) V^2 dV}{\int_0^\infty F_0(V) V^2 dV},$$

following from equations (30) and (34), we obtain

$$\eta_{\omega, \vec{k}} \approx \frac{\langle \hat{B}_{\omega, \vec{k}} \rangle}{i\Delta_{\omega, \vec{k}}} \left(1 + \frac{i\langle \hat{D}_{\omega, \vec{k}} \hat{B}_{\omega, \vec{k}} \rangle}{\Delta_{\omega, \vec{k}} \langle \hat{B}_{\omega, \vec{k}} \rangle} \right) \phi_{\omega, \vec{k}}, \quad (44)$$

where the speed averaging of any operator or function \hat{A} is defined as

$$\langle \hat{A} \rangle \equiv \frac{4\pi}{n_0} \int_0^\infty (\hat{A} F_0(V)) V^2 dV = \frac{\int_0^\infty (\hat{A} F_0(V)) V^2 dV}{\int_0^\infty F_0(V) V^2 dV}. \quad (45)$$

Expressing $\phi_{\omega, \vec{k}}$ again to the first-order accuracy with respect to the small parameter $|\langle \hat{D}_{\omega, \vec{k}} \hat{B}_{\omega, \vec{k}} \rangle|/|\Delta_{\omega, \vec{k}} \langle \hat{B}_{\omega, \vec{k}} \rangle|$ we obtain equation (52) from Dimant and Sudan (1995a):

$$\phi_{\omega, \vec{k}} \approx \left(\frac{i\Delta_{\omega, \vec{k}}}{\langle \hat{B}_{\omega, \vec{k}} \rangle} + \frac{\langle \hat{D}_{\omega, \vec{k}} \hat{B}_{\omega, \vec{k}} \rangle}{\langle \hat{B}_{\omega, \vec{k}} \rangle^2} \right) \eta_{\omega, \vec{k}}. \quad (46)$$

Combining equations (31) and (46), we obtain the FBI dispersion relation:

$$\frac{\Omega_{\omega, \vec{k}} [(1 - \kappa_i^2) \Omega_{\omega, k} + i\nu_{in}(1 + \kappa_i^2)]}{k^2 V_{Ti}^2} = 1 + \frac{1}{\beta_T} \left(\frac{\langle \hat{D}_{\omega, \vec{k}} \hat{B}_{\omega, \vec{k}} \rangle}{\langle \hat{B}_{\omega, \vec{k}} \rangle^2} + \frac{i\Delta_{\omega, \vec{k}}}{\langle \hat{B}_{\omega, \vec{k}} \rangle} \right), \quad (47)$$

which generalizes equation (58) from Dimant and Sudan (1995a) for general $F_0(V)$ and arbitrary ion magnetization.

The differential operators $\hat{D}_{\omega, \vec{k}}$ and $\hat{B}_{\omega, \vec{k}}$ are defined by equation (40). The terms proportional to \vec{E}_0 are crucial for the ETI, but for the FBI they play no role, so that we can reduce these operators to simpler expressions,

$$\hat{D}_{\omega, \vec{k}} \Rightarrow \frac{k_\perp^2 V^2 m_e \psi_e(V)}{3m_i \nu_{in}}, \quad \hat{B}_{\omega, \vec{k}} \Rightarrow -\frac{k_\perp^2 T_{e0}}{3m_i \nu_{in}} V \psi_e(V) \frac{d}{dV}, \quad (48)$$

where

$$\psi_e(V) \equiv \frac{\nu_{en}(V) \nu_{in}}{\omega_{ec} \omega_{ic}} \left(1 + \frac{k_\parallel^2 \omega_{ec}^2}{k_\perp^2 \nu_{en}^2(V)} \right) \quad (49)$$

is the kinetic analog of the standard fluid-model parameter ψ defined by equation (4). The reduced expression for $\hat{D}_{\omega, \vec{k}}$ fully agrees with equation (53) from Dimant and Sudan (1995a) after neglecting in that equation the term $\propto \zeta_{\omega, \vec{k}}$. At the same time, the operator $\hat{B}_{\omega, \vec{k}}$ can be reduced to Dimant and Sudan (1995a, equation (54)), only for Maxwellian $F_0(V)$. For general $F_0(V)$, in accord with equation (45), we obtain after integration by parts:

$$\begin{aligned} \langle \hat{B}_{\omega, \vec{k}} \rangle &= \frac{4\pi T_{e0} k_\perp^2}{3n_0 m_i \nu_{in}} \int_0^\infty F_0(V) \frac{d(V^3 \psi_e)}{dV} dV, \\ \langle \hat{D}_{\omega, \vec{k}} \hat{B}_{\omega, \vec{k}} \rangle &= \frac{4\pi T_{e0} m_e k_\perp^4}{9n_0 m_i^2 \nu_{in}^2} \int_0^\infty F_0(V) \frac{d(V^5 \psi_e^2)}{dV} dV. \end{aligned} \quad (50)$$

Under conditions of equation (41), in both sides of dispersion equation (47) the imaginary parts dominate. This allows us to easily separate the wave phase-velocity relation, $\omega_r(\vec{k})$, from the wave growth/damping relation, $\gamma(\vec{k})$.

The wave phase-velocity relation is obtained to the zeroth-order accuracy, after neglecting the small real parts, as well as small γ in $\omega = \omega_r + i\gamma$. This yields:

$$\omega_r = \frac{\vec{k} \cdot [\vec{V}_0 + (1 + \kappa_i^2)\tilde{\psi}\vec{V}_{i0}]}{1 + (1 + \kappa_i^2)\tilde{\psi}}, \quad (51)$$

where the constant parameter

$$\tilde{\psi} = \frac{\beta_T \nu_{in} \langle \hat{B}_{\omega, \vec{k}} \rangle}{k^2 V_{Ti}^2} = \frac{4\pi}{3n_0} \int_0^\infty F_0(V) \frac{d(V^3 \psi_e)}{dV} dV \quad (52)$$

unlike $\psi_e(V)$, generalizes the conventional parameter ψ for the entire electron population. Equations (32) and (51) yield the real part of $\Omega_{\omega, \vec{k}}$:

$$(\Omega_{\omega, \vec{k}})_r = \omega_r - \vec{k} \cdot \vec{V}_{i0} \approx \frac{\vec{k} \cdot \vec{U}}{1 + (1 + \kappa_i^2)\tilde{\psi}}, \quad (53a)$$

$$\vec{U} \equiv \vec{V}_0 - \vec{V}_{i0} \approx \left(\vec{V}_0 - \frac{e\vec{E}_0}{m_i \nu_{in}} \right) / (1 + \kappa_i^2). \quad (53b)$$

To the first-order accuracy, equation (47) yields:

$$\gamma \approx \frac{\tilde{\psi} \left[(1 - \kappa_i^2)(\Omega_{\omega, \vec{k}})_r^2 - k^2 \tilde{C}_s^2 \right]}{(1 + \tilde{\psi})\nu_{in}}, \quad (54)$$

where \tilde{C}_s is a modified ion-acoustic speed,

$$\tilde{C}_s^2 = V_{Ti}^2 + \frac{\langle \hat{D}_{\omega, \vec{k}} \hat{B}_{\omega, \vec{k}} \rangle V_{Ti}^2}{\beta_T \langle \hat{B}_{\omega, \vec{k}} \rangle^2}. \quad (55)$$

Using equation (50), the second term in the RHS of equation (55) can be written as

$$\begin{aligned} \frac{\langle \hat{D}_{\omega, \vec{k}} \hat{B}_{\omega, \vec{k}} \rangle V_{Ti}^2}{\beta_T \langle \hat{B}_{\omega, \vec{k}} \rangle^2} &= \frac{m_e n_0}{4\pi m_i} \frac{\int_0^\infty F_0(V) [d(V^5 \psi_e^2)/dV] dV}{\left(\int_0^\infty F_0(V) [d(V^3 \psi_e)/dV] dV \right)^2} \\ &= \frac{4\pi}{9n_0 \tilde{\psi}^2} \frac{m_e}{m_i} \int_0^\infty F_0(V) \frac{d(V^5 \psi_e^2)}{dV} dV. \end{aligned} \quad (56)$$

Equations (51) and (55) totally agree with equations (5) and (6) from Dimant and Milikh (2003) after replacing there the standard parameters ψ and C_s^2 with $\tilde{\psi}$ and \tilde{C}_s^2 , respectively. Notice that if the ion magnetization is sufficiently high, $\kappa_i > 1$, then the FBI driving mechanism, described in equation (54) by the term $(1 - \kappa_i^2)(\Omega_{\omega, \vec{k}})_r^2$, becomes stabilizing, as discussed in detail in Dimant and Oppenheim (2004). This happens above the magnetization boundary, $\kappa_i = 1$, which at the high-latitude ionosphere is located about 120 km of altitude (e.g., Dimant & Oppenheim, 2004, Fig. 5). In this paper, we will restrict our analysis to lower E-region altitudes where $\kappa_i < 1$.

We can rewrite the expression for the modified ion-acoustic speed, \tilde{C}_s , in a more traditional way as

$$\tilde{C}_s = \left(\frac{T_i + T_{\text{eff}}}{m_i} \right)^{1/2}, \quad T_{\text{eff}} = \frac{4\pi m_e}{9n_0 \tilde{\psi}^2} \int_0^\infty F_0(V) \frac{d(V^5 \psi_e^2)}{dV} dV. \quad (57)$$

Emphasize that \tilde{C}_s is not the actual ion-acoustic speed because in the highly dissipative lower ionosphere no ion-acoustic wave can survive for a time duration $\gtrsim \nu_{in}^{-1}$. For ion-acoustic waves, the collisional damping is even more detrimental than the collisionless

ion Landau damping at much higher ionospheric altitudes (if there $T_e \sim T_i$). In the highly dissipative E-region ionosphere, the analogs of the ion-acoustic-like waves are precisely the compression/decompression waves driven by the FBI and other plasma instabilities. These waves, however, can survive for a time duration much longer than ν_{in}^{-1} only because they are sustained by the external DC electric field, $\vec{E}_0 \perp \vec{B}$.

For constant ν_{en} (and hence for constant ψ_e), the above expressions reduce to the fluid-model FBI wave phase velocity and growth/damping rate relations. Indeed, in this case equation (52) yields $\tilde{\psi} = \psi_e = \psi$, so that equation (51) reduces to the fluid-model phase-velocity relation, see, e.g., equation (5) from Dimant and Milikh (2003), even for arbitrary background electron distribution function $F_0(V)$. For constant ψ_e , equation (54) reduces to fluid-model equation (6) from Dimant and Milikh (2003) for isothermal ions and adiabatic electrons,

$$\gamma = \frac{\psi[(1 - \kappa_i^2)(\Omega_{\omega, \vec{k}})_r^2 - k^2 C_s^2]}{(1 + \psi)\nu_{in}}, \quad C_s^2 = \frac{T_i + (5/3)T_{\text{tot}}}{m_i}, \quad (58)$$

where T_{tot} is defined by equation (6c). In reality, however, the kinetic quantity ν_{en} is strongly velocity-dependent, so that the exact form of the omnidirectional function $F_0(V)$ does really matter.

The fact that for constant ν_{en} the electron temperature term in C_s^2 includes the single-atom adiabaticity coefficient 5/3 is associated with the fact that we have neglected here the frictional heating and the corresponding collisional cooling of electrons. This approximation works for waves having sufficiently high wave frequencies, $\omega, kV_0 \gg \delta_{en}\nu_{en}$, while still satisfying the low-frequency, long-wavelength conditions imposed by equation (41). Here $\delta_{en} \simeq (2-4) \times 10^{-3}$ is the mean relative fraction of collisional losses of the electron energy during one $e-n$ collision (Gurevich, 1978; Dimant & Sudan, 1995a). In the opposite limit of very low-frequency, long-wavelength waves, $\omega, kV_0 \ll \delta_{en}\nu_{en}$, the electron thermal behavior is mostly determined by the heating/cooling balance, so that the factor 5/3 disappears and the destabilizing ETI mechanism for the optimal \vec{k} directions becomes efficient (Dimant & Sudan, 1995b, 1995c, 1997). The net result of this change is that the minimum threshold field is reached for longer-wavelength waves than for those prone to the pure FBI excitation.

The linear instability develops if the DC electric field exceeds the threshold field determined by $\gamma = 0$. According to equations (53) and (54), this yields the threshold parameters

$$\frac{E_{\text{Thr}}}{B} = V_{\text{Thr}} = \frac{(1 + \kappa_i^2) [1 + (1 + \kappa_i^2)\tilde{\psi}]}{(\cos \theta - \kappa_i \sin \theta) \sqrt{1 - \kappa_i^2}} \tilde{C}_s,$$

where θ is the angle between the wavevector \vec{k} and the $\vec{E}_0 \times \vec{B}$ -drift direction (the ‘‘flow’’ angle).

Crucial for the onset of the FBI is the minimum threshold field at a given location. The driving field and the corresponding $\vec{E}_0 \times \vec{B}$ -drift speed reach their minimal values at the optimal direction of the wavevector, $\vec{k} \parallel \vec{U}$, corresponding to $\theta = -\arctan \kappa_i$ and $k_{\parallel} = 0$:

$$\begin{aligned} \frac{(E_{\text{Thr}})_{\text{min}}}{B} &= (V_{\text{Thr}})_{\text{min}} = \sqrt{\frac{1 + \kappa_i^2}{1 - \kappa_i^2}} [1 + (1 + \kappa_i^2)\tilde{\psi}] \tilde{C}_s \\ &= \sqrt{\frac{1 + \kappa_i^2}{1 - \kappa_i^2}} \left[1 + (1 + \kappa_i^2) \frac{I_1}{3I_0} \right] \left(\frac{T_i}{m_i} + \frac{m_e I_0 I_2}{m_i I_1^2} \right)^{1/2}, \end{aligned} \quad (59)$$

where in the last equality we expressed $\tilde{\psi}$ (for $k_{\parallel} = 0$) and \tilde{C}_s in terms of the following integral parameters:

$$I_0 = \frac{n_0}{4\pi} = \int_0^{\infty} F_0 V^2 dV = \frac{\sqrt{2}}{m_e^{3/2}} \int_0^{\infty} F_0 \sqrt{\mathcal{E}} d\mathcal{E}, \quad (60a)$$

$$I_1 = \int_0^{\infty} F_0 \frac{d(V^3 \psi_e)}{dV} dV = \left(\frac{2}{m_e}\right)^{3/2} \int_0^{\infty} F_0 \frac{d(\mathcal{E}^{3/2} \psi_e)}{d\mathcal{E}} d\mathcal{E}, \quad (60b)$$

$$I_2 = \int_0^{\infty} F_0 \frac{d(V^5 \psi_e^2)}{dV} dV = \left(\frac{2}{m_e}\right)^{5/2} \int_0^{\infty} F_0 \frac{d(\mathcal{E}^{5/2} \psi_e^2)}{d\mathcal{E}} d\mathcal{E}. \quad (60c)$$

In the two equivalent forms for each I_k , $k = 0, 1, 2$, both F_0 and ψ_e should be taken as functions of either the electron speed V or the corresponding kinetic energy, $\mathcal{E} = m_e V^2/2$, depending on the integration variable.

It is conventional to express the distribution function and collision frequencies in terms of the electron kinetic energy, rather than of the electron speed, so that the integral forms in terms of \mathcal{E} are more convenient for specific calculations. The form of equation (59) in terms of I_k is convenient because it makes the threshold field totally insensitive to the normalization of F_0 since, in the relevant fractions, the common coefficients in different I_k cancel. This allows one to pick an arbitrary (but common for all I_k) normalization of the distribution function, provided F_0 includes the entire electron population that consists of the thermal bulk and the superthermal tail.

If both $\tilde{\psi} = (1 + \kappa_i^2)I_1/(3I_0)$ and κ_i are small (this dual condition is usually satisfied at altitudes between 100 and 110 km) then equation (59) reduces to a simpler relation,

$$\frac{(E_{\text{Thr}})_{\min}}{B} = (V_{\text{Thr}})_{\min} \approx \left(\frac{T_i}{m_i} + \frac{m_e I_0 I_2}{m_i I_1^2}\right)^{1/2}. \quad (61)$$

In this case, $(E_{\text{Thr}})_{\min}$ becomes insensitive to the normalization of the function ψ_e as well. This allows one to simultaneously replace in all integrals I_k the energy-dependent function ψ_e with merely the e - n collision frequency, ν_{en} , so that for $\psi, \kappa_i \ll 1$ we have

$$\begin{aligned} \frac{(E_{\text{Thr}})_{\min}}{B} &= (V_{\text{Thr}})_{\min} \approx \left(\frac{T_i + T_{\text{eff}}}{m_i}\right)^{1/2}, \\ T_{\text{eff}} &= \frac{\left(\int_0^{\infty} F_0(\mathcal{E}) \sqrt{\mathcal{E}} d\mathcal{E}\right) \int_0^{\infty} F_0(\mathcal{E}) [d(\mathcal{E}^{5/2} \nu_{en}^2(\mathcal{E})) / d\mathcal{E}] d\mathcal{E}}{\left\{\int_0^{\infty} F_0(\mathcal{E}) [d(\mathcal{E}^{3/2} \nu_{en}(\mathcal{E})) / d\mathcal{E}] d\mathcal{E}\right\}^2}. \end{aligned} \quad (62)$$

In the constant- ν_{en} limit, the effective FB-threshold temperature reduces to

$$(T_{\text{eff}})_{\nu_{en}=\text{const}} = \frac{10}{9} \frac{\int_0^{\infty} F_0(\mathcal{E}) \mathcal{E}^{3/2} d\mathcal{E}}{\int_0^{\infty} F_0(\mathcal{E}) \sqrt{\mathcal{E}} d\mathcal{E}}. \quad (63)$$

For Maxwellian EDF, $F_0(\mathcal{E}) \propto \exp(-\mathcal{E}/T_{e0})$, this further reduces to $(5/3)T_{e0}$, in full accord with equation (58). For the general, non-Maxwellian EDF, e.g., for the combined cold bulk electrons and SE, equation (63) would correspond to merely including the total electron pressure.

The main result of our FBI linear analysis for general $f_e(\vec{V}) \approx F_0(V)$ is given by equations (51), (54), and (59); the following relations just represent various simplifications. It is to be noted, however, that at altitudes closely approaching the magnetization boundary, $\kappa_i = 1$, the effect of ion-thermal instability (ITI) driving becomes tangible (Dimant & Oppenheim, 2004). The ITI driving modifies both the optimum angles of the instability onset and the threshold field values. Furthermore, the ITI driving even extends the unstable range of altitudes by a few kilometers above the magnetization boundary, where the pure FBI mechanism becomes stabilizing. Unlike the ETI mechanism, the

ITI mechanism destabilizes waves largely in the same wavelength range as does the FBI mechanism, so that the effect of ITI driving is inseparable from the FBI. We have not included in the present analysis any thermal effects because that would make our theoretical treatment much more complicated. This may be a subject of a future work.

4.3 Specific Calculations for Superthermal Electrons Produced by Electron Precipitation

In order to estimate the contribution of the superthermal energy tail formed by precipitating electrons, we apply the equations derived above to specific calculations of the FBI threshold. We separate the dominant omnidirectional part of the total electron velocity distribution, $f_e(\vec{V}) \approx F_0(\mathcal{E})$, into two distinct components,

$$F_0(\mathcal{E}) \approx F_{\text{TB}}(\mathcal{E}) + F_{\text{SE}}(\mathcal{E}), \quad (64)$$

namely, the undisturbed thermal bulk described by the Maxwellian distribution,

$$F_{\text{TB}}(\mathcal{E}) = n_{\text{TB}} \left(\frac{m_e}{2\pi T_{\text{TB}}} \right)^{3/2} \exp\left(-\frac{\mathcal{E}}{T_{\text{TB}}}\right), \quad (65)$$

and the superthermal EDF, $F_{\text{SE}}(\mathcal{E})$, calculated numerically using the kinetic code STET, as described above in sections 2.2 and 3. The Maxwellian thermal bulk electron distribution, F_{TB} , is fully determined by the values of the undisturbed temperature, T_{TB} , and density, n_{TB} . We take these values from ionospheric models, as described in section 3. The superthermal EDF, $F_{\text{SE}}(\mathcal{E})$, was calculated by STET in the energy range between 1 eV and 30 keV. In the low-energy range below 1 eV, the main contributions into all relevant integrals come almost exclusively from Maxwellian $F_{\text{TB}}(\mathcal{E})$, while the entire energy range above 1 eV is overwhelmingly dominated by $F_{\text{SE}}(\mathcal{E})$. This allows us to disregard possible inaccuracies of the EDF within the interface energy range of $\mathcal{E} \sim 1$ eV.

For simplicity, we will do our specific calculations for the intermediate E-region altitudes where both conditions $\psi \ll 1$ and $\kappa_i \ll 1$ hold. Since $\psi \propto \kappa_i^{-1}$, there is an overlapping altitude range, roughly between 100 and 110 km, where both conditions hold concurrently. In this case, the minimum threshold field is approximately given by equation (62), where normalizations of both $F_0(\mathcal{E})$ and $\nu_{en}(\mathcal{E})$ can be ignored, provided they are common across all four integrals in the expression for T_{eff} .

We start by approximating analytically the function $\nu_{en}(\mathcal{E}) = n_n \sigma_{en}(\mathcal{E}) V(\mathcal{E})$, where n_n is the neutral density and $\sigma_{en}(\mathcal{E})$ is the energy-dependent e - n collision momentum transfer cross section. We need to fit $\nu_{en}(\mathcal{E})$ by a continuous analytic function of the electron energy, \mathcal{E} , because the expression for the effective temperature, (62), involves the energy derivative of $\nu_{en}(\mathcal{E})$.

At the altitudes of interest, the neutral atmosphere consists mostly of the molecular nitrogen and oxygen ($\sim 80\%$ of N_2 and $\sim 20\%$ of O_2), so that N_2 is more abundant. Besides, the e - N_2 collisional cross section vastly dominates over the e - O_2 collisional cross section (e.g., Solomon et al., 1988). This allows us to neglect the e - O_2 collisions and approximate the entire neutral population by the nitrogen molecules. In this approximation, the e - n cross section $\sigma_{en}(\mathcal{E})$ becomes a universal function of the electron energy \mathcal{E} , see Fig. 2. For this paper, we have approximated the data presented in Itikawa (2006, Table 2), with an addition of the top value of $\mathcal{E} = 10$ keV from Solomon et al. (1988). The analytic expression is given by $\sigma_{en}(\mathcal{E}) = 10^{-16} \text{cm}^2 \times \Sigma(\mathcal{E})$, where the piecewise function $\Sigma(\mathcal{E})$ is expressed in the polynomial-fractional form $\Sigma(\mathcal{E}) = \sum_{k=0}^m \alpha_k \mathcal{E}^k / \sum_{p=0}^m \beta_p \mathcal{E}^p$ with \mathcal{E} expressed in eV. The details of this approximation are given in Appendix A. The universal approximation given by equation (A1) can be effectively employed in many kinetic problems involving collisions of electrons with molecules N_2 .

The effective temperature T_{eff} is insensitive to the normalization of the collision frequency $\nu_{en}(\mathcal{E}) = n_n \sigma_{en}(\mathcal{E}) (2\mathcal{E}/m_e)^{1/2}$, so that we can replace the latter with $\Sigma(\mathcal{E})\sqrt{\mathcal{E}}$,

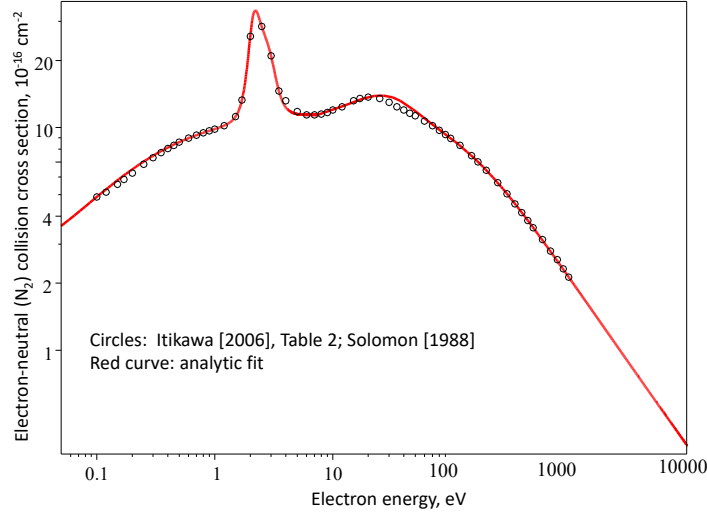


Figure 2. The e - N_2 collision cross-section as a function of the electron energy, \mathcal{E} : (Itikawa, 2006; Solomon et al., 1988, Table 2) and analytic fitting, $\sigma_{en}(\mathcal{E}) = 10^{-16}\text{cm}^2 \times \Sigma(\mathcal{E})$, with $\Sigma(\mathcal{E})$ given by equation (A1).

and obtain:

$$T_{\text{eff}} = \frac{K_1 K_2}{K_3} \quad (66)$$

where

$$\begin{aligned} K_1 &= \int_0^\infty F_0(\mathcal{E}) \sqrt{\mathcal{E}} d\mathcal{E}, \\ K_2 &= \int_0^\infty F_0(\mathcal{E}) \frac{d(\mathcal{E}^{7/2} \Sigma^2(\mathcal{E}))}{d\mathcal{E}} d\mathcal{E}, \\ K_3 &= \int_0^\infty F_0(\mathcal{E}) \frac{d(\mathcal{E}^2 \Sigma(\mathcal{E}))}{d\mathcal{E}} d\mathcal{E}. \end{aligned} \quad (67)$$

and the total distribution function of equation (64) can be written as

$$F_0(\mathcal{E}) = \xi \exp(-31.446\mathcal{E}) + \eta F_{\text{SE}}(\mathcal{E}),$$

with $\xi = 3.931 \times 10^{-7}$, $\eta = 1.616 \times 10^{-19}$, and \mathcal{E} in eV. The normalization coefficients ξ and η provide the distribution function to be measured in s^3m^{-6} .

For a specific STET simulation, we pick the Maxwell input with the energy flux $10 \text{ erg cm}^{-2}\text{s}^{-1}$, the characteristic energy 30 keV, at the 110 km of altitude. The simulated electron distribution function in the superthermal range of energies between 1 eV and 30 keV is reasonably well approximated by a piecewise expression given by equation (B2).

Using these analytic fits given by equations (A1) and (B2), after all numeric integrations, we obtain

$$K_1 \approx 1.976 \times 10^{-21}, \quad K_2 \approx 2.676 \times 10^{-19}, \quad K_3 \approx 3.665 \times 10^{-21}. \quad (68)$$

In K_1 and K_3 , the thermal bulk distribution, $F_{\text{TB}}(\mathcal{E})$, vastly dominates the total integrals, whereas in K_2 , due to the higher power of \mathcal{E} in the integrand, on the contrary, the superthermal distribution $F_{\text{SE}}(\mathcal{E})$ determines essentially the entire integral value.

Equation (67) leads to the effective temperature $T_{\text{eff}} \approx 39.4$ eV (while the effective electron temperature based on the total electron pressure, see equation (63), would yield a much smaller value of 0.11 eV). This extremely high value of T_{eff} increases the regular FBI threshold corresponding to $T_{e,i} = 300$ K (about 0.026 eV), $E_{\text{Thr0}} = 20[B/(5 \times 10^4 nT)]$ mV/m, by a significant factor (almost 30). This results in the enormous threshold field, $E_{\text{Thr}} \approx [(T_i + T_{\text{eff}})/600 \text{ K}]^{1/2} E_{\text{Thr0}} \approx 0.55[B/(5 \times 10^4 nT)]$ V/m. To excite the FBI under these conditions, the convection DC electric field mapped from magnetosphere down to the E-region altitudes must exceed this field. At the ionosphere altitudes, such huge convection electric fields, that would correspond to the $\vec{E} \times \vec{B}$ -drift speed as large as almost 11 km/s, have never been reported. This means that for this level of precipitation, the strongly elevated FBI threshold can hardly be reached during extreme geomagnetic storm events, and even during modest ones.

This specific simulation was performed for a relatively strong precipitation with the mean energy flux $\Phi_{\mathcal{E}} = 10 \text{ erg cm}^{-2} \text{ s}^{-1}$. As we discussed in section 3, any superthermal particle-energy-integrated characteristics will be proportional to $\Phi_{\mathcal{E}}$. Since the contribution of the superthermal energy tail to the integrals $K_{1,3}$ is negligible, whereas K_2 is determined almost entirely by $F_{\text{TB}}(\mathcal{E})$, the effective FBI threshold “temperature”, T_{eff} , is in direct proportion to the energy flux, $T_{\text{eff}} \propto \Phi_{\mathcal{E}}$. Thus we can generalize the previous result as $T_{\text{eff}} \approx 39.4(\Phi_{\mathcal{E}}/10 \text{ erg cm}^{-2} \text{ s}^{-1})$ eV.

Furthermore, according to Figure 1, at a given E-region altitude (e.g., 110 km) the superthermal EDF does not vary significantly in the broad range of plasmashet electron characteristic energies, \mathcal{E}_0 , between 5 keV and 30 keV (at least, for the Maxwell precipitation input). This allows us to roughly use the approximation of equation (B1) to be a ‘universal’ EDF within the energy domain, say, between 1 eV and a given SE cut-off energy \mathcal{E}_{max} with the zero values outside (in the above calculation, $\mathcal{E}_{\text{max}} = 20$ keV). This allows us to obtain an explicit analytic expression for the SE-dominated effective temperature.

The idea of this calculation is as follows. Assuming \mathcal{E}_{max} to be in the energy domain between 1 keV and 30 keV, we can separate the major integral K_2 into two parts: a lower-energy part between 1 eV and 1 keV and the higher-energy remainder. The lower-energy part can be calculated numerically, which is done above, in equations (1), (2). This calculation yields a specific number. For the remaining integral between 1 keV and \mathcal{E}_{max} , we can use the large-energy asymptotics of both functions $F_0(\mathcal{E})$ and $\Sigma(\mathcal{E})$,

$$F_0(\mathcal{E}) = Q(\mathcal{E}) \approx \beta \left(1 + \frac{A}{\mathcal{E}} + \frac{B}{\mathcal{E}^2} \right),$$

$$\Sigma(\mathcal{E}) = S(\mathcal{E}) \approx m \left(\frac{1}{\mathcal{E}} \right)^{\frac{3}{4}} \left(1 + \frac{p}{\mathcal{E}} \right),$$

where

$$\beta = 0.025, \quad A = 634.6, \quad B = 2.721 \times 10^6,$$

$$m = 373, \quad p = 35.21.$$

For energies above 1 eV these asymptotics are very close to the original functions. Combining the two parts of the integral, after dropping some small and inconsequential terms, we obtain for the total SE contribution into K_2 a simple algebraic function of \mathcal{E}_{max} :

$$K_2 \approx 5.622 \times 10^{-28} \mathcal{E}_{\text{max}}^2 + 7.531 \times 10^{-25} \mathcal{E}_{\text{max}}$$

$$+ 3.085 \times 10^{-21} \ln \mathcal{E}_{\text{max}} - 4.966 \times 10^{-21}. \quad (69)$$

In the entire energy domain of 1-30 keV, the integrals $K_{1,3}$ are vastly dominated by the cold bulk-electron energy distribution with the specific values given by equation (68),

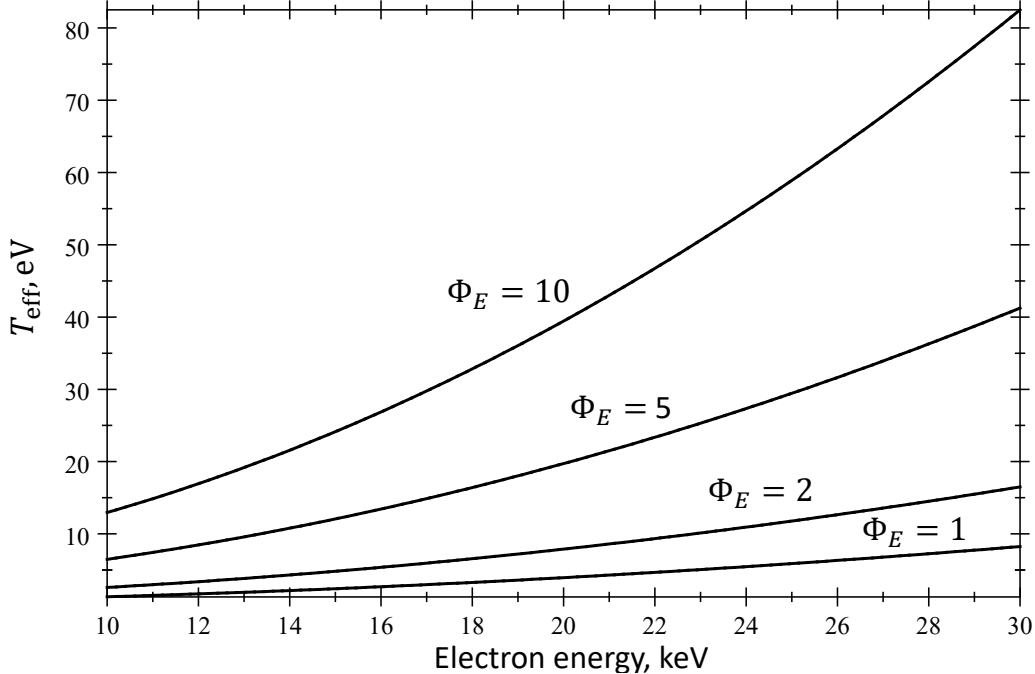


Figure 3. Effective temperature (in eV) vs. electron energy (in keV). The values of the energy flux, Φ_E (in $\text{erg cm}^{-2} \text{s}^{-1}$), are shown near the curves.

while K_2 , determined almost entirely by the SE energy distribution, is given by equation (69). As a result, we obtain

$$T_{\text{eff}}(\text{eV}) \approx 8.35 \times 10^{-2} \mathcal{E}_{\text{max}}^2 + 0.112 \mathcal{E}_{\text{max}} + 0.46 \ln \mathcal{E}_{\text{max}} + 2.43, \quad (70)$$

where, unlike the above, we express \mathcal{E}_{max} is in keV. In the particular case of $\mathcal{E}_{\text{max}} = 20$ keV, equation (70) reproduces the specific value of $T_{\text{eff}}(\text{eV}) \approx 39.4$ eV obtained above. Figure 3 shows the energy dependence given by equation (70) and similar for different values of the energy flux, Φ_E (the values of T_{eff} are proportional to Φ_E).

In this paper, we have restricted our treatment to the FBI, disregarding other instability drivers, such as the ETI and ITI driving mechanisms. The latter instabilities may reduce the instability threshold. We may include the other instability drivers in our future analysis, but one should hardly expect any drastic changes in the predicted increase of the instability threshold caused by strong electron precipitation.

In principle, the predicted effect of suppression of the E-region instabilities by strong electron precipitation is verifiable by observations. Unfortunately, there are almost no simultaneous collocated observations of electron precipitation and E-region irregularities caused by the FBI because such observations and their accurate interpretation represent a certain challenge [D. Hysell, private communication]. Nevertheless, we are aware of at least one work where the authors have reported on observations of collocated optical and radar auroras (Bahcivan et al., 2006). The data presented there indicate suppression of the FBI inside the auroral arc, vs. the arc edges where radar aurora still exists. In their conclusion 4, Bahcivan et al. (2006) state: “The radar aurora was often observed at the discrete arc boundary and suppressed inside the arc. Radar aurora could sometimes be seen inside an arc at the very peak of optical intensification.” The authors’ interpretation of the observed suppression is that within the arc the driving electric field might had been dramatically reduced due to the enhanced conductivity, so that the E-

field magnitude might have dropped below the regular FBI threshold value. While E-field reduction is a possible mechanism, one must also consider dramatically increased FBI threshold due to precipitating electrons within the arcs. In order to sustain or disprove our theory, more future observations with better statistics and more careful data analysis are needed.

5 Conclusions

During events of strong geomagnetic activity, most of the intense magnetospheric currents close through the high-latitude E-region ionosphere. At E-region altitudes between 100 and 120 km, strong DC electric, mapped down from the magnetosphere, can drive plasma instabilities, such as the Farley-Buneman instability (FBI) and others. These instabilities give rise to anomalous electron heating and enhanced plasma particle transport, affecting the global ionospheric conductances and, hence, the entire dynamics of the near-Earth's plasma.

During geomagnetic perturbations, strong electron precipitation also happens, resulting in Aurora and enhanced ionization. The regions of strong electric fields that drive E-region instabilities and the auroral regions of strong electron precipitation may overlap in space, so that the two effects might interact. This work shows that the intense electron precipitation can modify significantly the conditions necessary to drive the instability.

We have analyzed theoretically how strong electron precipitation affects the threshold conditions for the FBI driving. To this end, we performed a series of kinetic simulations of superthermal electrons, using the sophisticated kinetic code STET (Khazanov et al., 1993), using various kinds of the input particle fluxes. These simulations predict distributions of superthermal electrons in the energy range between 1 eV and 30 keV. While the total number density of the superthermal electrons (SE) is usually small compared to the total number density of the electron thermal bulk (TB), the total energy of the entire hot SE population is often many times that of the entire cold TB population.

This means that the SE total pressure, P_{SE} , exceeds dramatically the regular pressure of the dominant TB population, $P_{TB} = n_0 T_e$. Since the SE particle density is typically small compared to n_0 then the dominant SE pressure creates an effective plasma temperature in proportion to P_{SE} . The elevated electron temperature increases the particle diffusion and hence the instability threshold, thus suppressing the instability or at least reducing its efficiency. In order to quantify the threshold conditions, a naive viewpoint might suggest to just replace the regular electron temperature with the elevated effective temperature P_{SE}/n_0 in the conventional threshold conditions for the E-region instabilities.

The actual situation, however, turns out to be more complicated. Even an oversimplified three-fluid model, in which the TB and SE electron populations are treated as two different Maxwellian distribution functions, demonstrates that the FBI threshold field involves the e - n collision frequencies whose values differ dramatically for the two electron populations. The fact that the e - n collision frequency varies gradually with energy and cannot be reduced to just two distinct values means that a quantitative analysis of growth rates requires kinetic theory.

The kinetic theory developed here confirms that the strongly energy-dependent e - n collision frequency plays a crucial role in the FBI threshold conditions. The physical reason is that the instability threshold is determined by diffusive losses, where the Pedersen diffusion (i.e., diffusion along the total electrostatic field and perpendicular to the magnetic field) plays the principal role in low-frequency plasma density waves. The Pedersen diffusion coefficient of magnetized electrons is proportional to the e - n collision fre-

quency ν_{en} , so that for the general non-Maxwellian electron velocity distributions the energy dependence of ν_{en} cannot be canceled out. Furthermore, specific calculations for realistic conditions shows that the energy dependence of ν_{en} results in much more severe suppression of the instability compared to the naive model of the just pressure-dependent threshold: the effective “temperature” for the FBI threshold may exceed that determined by the modified electron pressure alone by more than order of magnitude.

While there is some observational evidence of the FBI suppression within the optically active arcs of intense electron precipitation, those observations cannot be considered as definite proof of our theory because alternative explanations also exist (Bahcivan et al., 2006). Nevertheless, we believe that our theoretical treatment is based on solid physical foundations, so that its major conclusion of possible dramatic suppression of E-region instabilities by precipitating electrons should be correct.

Appendix A Analytic approximation of the energy-dependent e-N₂ collision cross-section

In this appendix, we approximate analytically the energy-dependent cross-section of electron collisions with N₂ molecules. For $\sigma_{en}(\mathcal{E})$, we use the most up-to-date numerical model compiled by Itikawa (2006), which is in full agreement with the corresponding data published earlier by Solomon et al. (1988, Fig. A1a).

$$\Sigma(\mathcal{E}) = \begin{cases} \frac{a_0+a_1\mathcal{E}+a_2\mathcal{E}^2+a_3\mathcal{E}^3+a_4\mathcal{E}^4+a_5\mathcal{E}^5}{b_0+b_1\mathcal{E}+b_2\mathcal{E}^2+b_3\mathcal{E}^3+b_4\mathcal{E}^4+b_5\mathcal{E}^5} & \text{if } \mathcal{E} \leq 7.484, \\ \frac{A_0+A_1\mathcal{E}+A_2\mathcal{E}^2+373\mathcal{E}^3}{B_0+B_1\mathcal{E}+B_2\mathcal{E}^2+\mathcal{E}^{3.75}} & \text{if } \mathcal{E} > 7.484. \end{cases}, \quad (\text{A1})$$

Here the electron energy \mathcal{E} is expressed in eV and the numeric parameters a_k , b_p , A_k , and B_p ($k, p = 1, 2, 3, \dots$) are given by

$$\begin{aligned} a_0 &= 1.0, & a_1 &= 29.343\,718\,19, & a_2 &= -48.032\,970\,58, \\ b_0 &= 0.570\,827\,0397, & b_1 &= 1.773\,322\,602, & b_2 &= -3.690\,608\,199, \\ A_0 &= 40281607.78, & A_1 &= -151764.479\,1, & A_2 &= 13134.794\,16, \\ a_3 &= 28.820\,983\,19, & a_4 &= -7.611\,134\,714, & a_5 &= 0.755\,097\,368\,6, \\ b_3 &= 2.357\,341\,373, & b_4 &= -0.641\,715\,008\,1, & b_5 &= 0.06.479\,534\,438, \\ B_0 &= 4189550.095, & B_1 &= -117601.051\,2, & B_2 &= 3517.072\,043. \end{aligned} \quad (\text{A2})$$

Figure 2 shows that equation (A1) agrees with the published tabulated data almost perfectly. At the interface energy between the two pieces, $\mathcal{E}_c = 7.484$ eV, the function $\Sigma(\mathcal{E}_c) \approx 11.41$ is continuous but not smooth; the corresponding derivatives on both sides of \mathcal{E}_c differ by an order of magnitude, $d\Sigma/d\mathcal{E}|_{\mathcal{E}_c-\Delta} \approx 0.02$ and $d\Sigma/d\mathcal{E}|_{\mathcal{E}_c+\Delta} \approx 0.24$, where Δ is an infinitesimal positive number. According to equation (62), the derivatives of $\Sigma(\mathcal{E})$ are involved in the integrations, but both values of $d\Sigma/d\mathcal{E}$ around $\mathcal{E} = \mathcal{E}_c$ are so small that the inaccuracy caused by the fitting discontinuity is inconsequential. It is important that the analytical fit described by equations (A1) and (A2) describes adequately all major details of $\sigma_{en}(\mathcal{E})$, including the well-known N₂ vibrational excitation peak around 2.5 eV.

Appendix B Analytic approximation of the SE distribution function (Maxwell input $\Phi_{\mathcal{E}} = 10$ erg cm⁻²s⁻¹, 30 keV, 110 km)

In this appendix, we approximate analytically the STET-simulated distribution function for the Maxwell input with the energy flux 10 erg cm⁻²s⁻¹, the characteristic energy 30 keV, at the 110 km of altitude. The simulated electron distribution function in the superthermal range of energies between 1 eV and 30 keV is reasonably well approx-

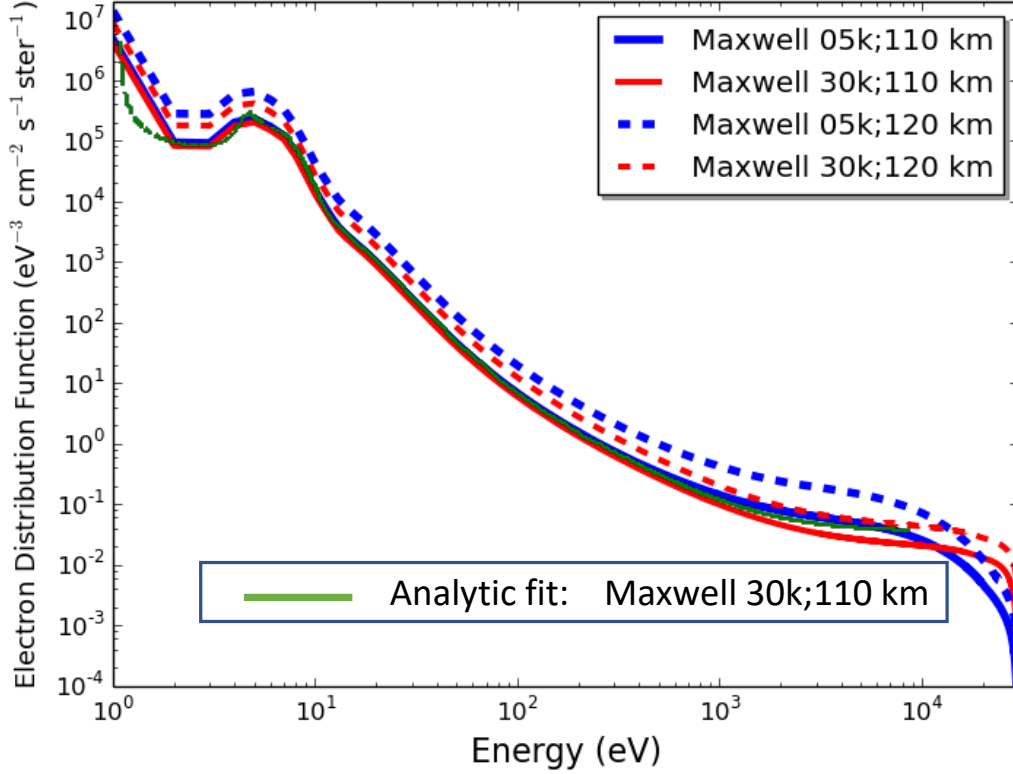


Figure B1. Analytic fit of superthermal electron energy distribution function (the green curve); the parameters are shown in the figure.

imated by a piecewise expression similar in form to equation (A1),

$$F_{\text{SE}}(\mathcal{E}) \approx \begin{cases} \frac{p_0 + p_1 \mathcal{E} + p_2 \mathcal{E}^2 + p_3 \mathcal{E}^3 + p_4 \mathcal{E}^4 + p_5 \mathcal{E}^5}{q_0 + q_1 \mathcal{E} + q_2 \mathcal{E}^2 + q_3 \mathcal{E}^3 + q_4 \mathcal{E}^4 + q_5 \mathcal{E}^5} & \text{if } \mathcal{E} \leq 10, \\ \frac{M_0 + M_1 \mathcal{E} + M_2 \mathcal{E}^2 + M_3 \mathcal{E}^3 + M_4 \mathcal{E}^4}{N_0 + N_1 \mathcal{E} + N_2 \mathcal{E}^2 + N_3 \mathcal{E}^3 + \mathcal{E}^4} & \text{if } \mathcal{E} > 10, \end{cases} \quad (\text{B1})$$

where \mathcal{E} is in eV,

$$\begin{aligned} p_0 &= 1.0, & p_1 &= -7.174838957, \\ p_2 &= 4.278098241, & p_3 &= -0.9365241978, \\ p_4 &= 8.411776876 \times 10^{-2}, & p_5 &= -2.740658004 \times 10^{-3}, \\ q_0 &= 1.837621454 \times 10^{-4}, & q_1 &= -3.191885523 \times 10^{-4}, \\ q_2 &= 1.713056278 \times 10^{-4}, & q_3 &= -4.093406764 \times 10^{-5}, \\ q_4 &= 4.586456085 \times 10^{-6}, & q_5 &= -2.0003 \times 10^{-7}, \end{aligned} \quad (\text{B2})$$

and

$$\begin{aligned} M_0 &= 488045957.3, & M_1 &= 8068167.375, & M_2 &= 73402.0464, \\ M_3 &= 24.85436516, & M_4 &= 0.025, & N_0 &= -1059681.101, \\ N_1 &= 207060.5108, & N_2 &= -13361.65483, & N_3 &= 359.5563169. \end{aligned} \quad (\text{B3})$$

This analytic fitting is shown in Fig. B1. This fitting matches the actual simulated data reasonably well, except the low-energy range of 1-2 eV and, to some degree, above $\mathcal{E} = 3$ keV. The former range plays no role, while the latter may introduce some error, but not very significant.

Acknowledgments

Work is supported by NASA LWS Grant #80NSSC19K0080.

References

- Bahcivan, H., Hysell, D. L., Larsen, M. F., & Pfaff, R. F. (2005, May). The 30 MHz imaging radar observations of auroral irregularities during the JOULE campaign. *Journal of Geophysical Research (Space Physics)*, *110*(A5), A05307. doi: 10.1029/2004JA010975
- Bahcivan, H., Hysell, D. L., Lummerzheim, D., Larsen, M. F., & Pfaff, R. F. (2006, December). Observations of colocated optical and radar aurora. *J. Geophys. Res.*, *111*(A12), A12308. doi: 10.1029/2006JA011923
- Banks, P. M., Chappell, C. R., & Nagy, A. F. (1974, April). A new model for the interaction of auroral electrons with the atmosphere: Spectral degradation, backscatter, optical emission, and ionization. *J. Geophys. Res.*, *79*(10), 1459-1470. doi: 10.1029/JA079i010p01459
- Bilitza, D., Altadill, D., Truhlik, V., Shubin, V., Galkin, I., Reinisch, B., & Huang, X. (2017, February). International Reference Ionosphere 2016: From ionospheric climate to real-time weather predictions. *Space Weather*, *15*(2), 418-429. doi: 10.1002/2016SW001593
- Buneman, O. (1963). Excitation of field aligned sound waves by electron streams. *Phys. Rev. Lett.*, *10*, 285-288.
- Dimant, Y. S., & Milikh, G. M. (2003, September). Model of anomalous electron heating in the E region: 1. Basic theory. *J. Geophys. Res.*, *108*, 5-1. doi: 10.1029/2002JA009524
- Dimant, Y. S., & Oppenheim, M. M. (2004). Ion thermal effects on E-region instabilities: Linear theory. *J. Atmos. & Solar Terr. Phys.*, *66*, 1655-1668.
- Dimant, Y. S., & Oppenheim, M. M. (2011, September). Magnetosphere-ionosphere coupling through E-region turbulence: 2. Anomalous conductivities and frictional heating. *J. Geophys. Res.*, *116*, A09304. doi: 10.1029/2011JA016649
- Dimant, Y. S., & Sudan, R. N. (1995a, April). Kinetic theory of low-frequency cross-field instability in a weakly ionized plasma. I. *Phys. Plasmas*, *2*, 1157-1168. doi: 10.1063/1.871394
- Dimant, Y. S., & Sudan, R. N. (1995b, April). Kinetic theory of low-frequency cross-field instability in a weakly ionized plasma. II. *Phys. Plasmas*, *2*, 1169-1181.
- Dimant, Y. S., & Sudan, R. N. (1995c). Kinetic theory of the Farley-Buneman instability in the E region of the ionosphere. *J. Geophys. Res.*, *100*, 14605-14624.
- Dimant, Y. S., & Sudan, R. N. (1997, February). Physical nature of a new cross-field current-driven instability in the lower ionosphere. *J. Geophys. Res.*, *102*, 2551-2564. doi: 10.1029/96JA03274
- Farley, D. T. (1963). A plasma instability resulting in field-aligned irregularities in the ionosphere. *J. Geophys. Res.*, *68*, 6083-6097.
- Forsythe, V. V., & Makarevich, R. A. (2015, October). Dual radar investigation of E region plasma waves in the southern polar cap. *J. Geophys. Res.*, *120*(10), 9132-9147. doi: 10.1002/2015JA021664
- Foster, J. C., & Erickson, P. J. (2000, October). Simultaneous observations of E-region coherent backscatter and electric field amplitude at F-region heights with the Millstone Hill UHF radar. *Geophys. Res. Lett.*, *27*, 3177-3180.
- Fukao, S., Yamamoto, M., Tsunoda, R. T., Hayakawa, H., & Mukai, T. (1998). The SEEK (Sporadic-E Experiment over Kyushu) campaign. *Geophys. Res. Lett.*, *25*, 1761-1764.
- Gurevich, A. V. (1978). Nonlinear phenomena in the ionosphere. *Springer Verlag, Springer Series on Physics Chemistry Space*, *10*.
- Hedin, A. E. (1991, February). Extension of the MSIS thermosphere model into the middle and lower atmosphere. *J. Geophys. Res.*, *96*(A2), 1159-1172. doi: 10.1029/90JA02125
- Hoh, F. C. (1963). Instability of penning-type discharge. *Phys. Fluids*, *6*, 1184.
- Hysell, D. L., Michhue, G., Larsen, M. F., Pfaff, R., Nicolls, M., Heinselman, C., & Bahcivan, H. (2008, July). Imaging radar observations of Farley Buneman

- waves during the JOULE II experiment. *Annales Geophysicae*, 26, 1837-1850.
- Itikawa, Y. (2006, March). Cross Sections for Electron Collisions with Nitrogen Molecules. *Journal of Physical and Chemical Reference Data*, 35(1), 31-53. doi: 10.1063/1.1937426
- Khazanov, G. V. (2011). *Kinetic Theory of the Inner Magnetospheric Plasma*. Springer, New York.
- Khazanov, G. V., Glocer, A., & Chu, M. (2021, May). Electron Energy Interplay in the Geomagnetic Trap Below the Auroral Acceleration Region. *Journal of Geophysical Research (Space Physics)*, 126(5), e28811. doi: 10.1029/2020JA028811
- Khazanov, G. V., Glocer, A., & Himwich, E. W. (2014, Jan). Magnetosphere-ionosphere energy interchange in the electron diffuse aurora. *J. Geophys. Res.*, 119(1), 171-184. doi: 10.1002/2013JA019325
- Khazanov, G. V., Glocer, A., Sibeck, D. G., Tripathi, A. K., Detweiler, L. G., Avanov, L. A., & Singhal, R. P. (2016, July). Ionosphere-magnetosphere energy interplay in the regions of diffuse aurora. *J. Geophys. Res.*, 121(7), 6661-6673. doi: 10.1002/2016JA022403
- Khazanov, G. V., Himwich, E. W., Glocer, A., & Sibeck, D. (2016). *The role of multiple atmospheric reflections in the formation of the electron distribution function in the diffuse aurora region*. AGU Monograph, 215.
- Khazanov, G. V., Liemohn, M. W., Gombosi, T. I., & Nagy, A. F. (1993, December). Non-steady-state transport of superthermal electrons in the plasmasphere. *Geophys. Res. Lett.*, 20, 2821-2824. doi: 10.1029/93GL03121
- Khazanov, G. V., Sibeck, D. G., & Chu, M. (2021). Magnetosphere-ionosphere coupling of precipitating electrons and ionospheric conductance. In H. H. R. Maggiolo N. André & D. T. Welling (Eds.), *Space physics and aeronomy collection, volume 2: Magnetospheres in the solar system* (Vol. 259). New York: American Geophysical Union. Published by John Wiley & Sons, Inc.
- Khazanov, G. V., Sibeck, D. G., & Zesta, E. (2017, April). Major pathways to electron distribution function formation in regions of diffuse aurora. *J. Geophys. Res.*, 122(4), 4251-4265. doi: 10.1002/2017JA023956
- Maeda, K., Tsuda, T., & Maeda, H. (1963). Theoretical interpretation of the equatorial sporadic E layers. *Phys. Rev. Lett.*, 11, 406-409.
- Marklund, G. T., Sadeghi, S., Karlsson, T., Lindqvist, P.-A., Nilsson, H., Forsyth, C., ... Pickett, J. (2011, February). Altitude Distribution of the Auroral Acceleration Potential Determined from Cluster Satellite Data at Different Heights. *Phys. Rev. Lett.*, 106(5), 055002. doi: 10.1103/PhysRevLett.106.055002
- McIntosh, R. C., & Anderson, P. C. (2014, December). Maps of precipitating electron spectra characterized by Maxwellian and kappa distributions. *J. Geophys. Res.*, 119(A18), 10. doi: 10.1002/2014JA020080
- Merkin, V. G., Milikh, G., Papadopoulos, K., Lyon, J., Dimant, Y. S., Sharma, A. S., ... Wiltberger, M. (2005, November). Effect of anomalous electron heating on the transpolar potential in the LFM global MHD model. *Geophysical Research Letters*, 32, 22101. doi: 10.1029/2005GL023315
- Milikh, G. M., & Dimant, Y. S. (2003, September). Model of anomalous electron heating in the E region: 2. Detailed numerical modeling. *Journal of Geophysical Research (Space Physics)*, 108(A9), 1351. doi: 10.1029/2002JA009527
- Newell, P. T., Lee, A. R., Liou, K., Ohtani, S.-I., Sotirelis, T., & Wing, S. (2010, September). Substorm cycle dependence of various types of aurora. *Journal of Geophysical Research (Space Physics)*, 115(A9), A09226. doi: 10.1029/2010JA015331
- Newell, P. T., Sotirelis, T., & Wing, S. (2009, September). Diffuse, monoenergetic, and broadband aurora: The global precipitation budget. *Journal of Geophysical Research (Space Physics)*, 114, A09207. doi: 10.1029/2009JA014326

- Oppenheim, M., Dimant, Y., Longley, W., & Fletcher, A. C. (2020, March). Newly Discovered Source of Turbulence and Heating in the Solar Chromosphere. *Astrophys. J.*, *891*(1), L9. doi: 10.3847/2041-8213/ab75bc
- Oppenheim, M. M., & Dimant, Y. S. (2013, March). Kinetic simulations of 3-D Farley-Buneman turbulence and anomalous electron heating. *J. Geophys. Res.*, *118*, 1306-1318. doi: 10.1002/jgra.50196
- Pfaff, R. F., Kelley, M. C., Fejer, B. G., Kudeki, E., Carlson, C. W., Pedersen, A., & Hausler, B. (1984, January). Electric field and plasma density measurements in the auroral electrojet. *J. Geophys. Res.*, *89*(A1), 236-244. doi: 10.1029/JA089iA01p00236
- Pfaff, R. F., Kelley, M. C., Kudeki, E., Fejer, B. G., & Baker, K. D. (1987, December). Electric field and plasma density measurements in the strongly driven daytime equatorial electrojet. 2. Two-stream waves. *J. Geophys. Res.*, *92*(A12), 13597-13612. doi: 10.1029/JA092iA12p13597
- Pfaff, R. F., Sahr, J., Providakes, J. F., Swartz, W. E., Farley, D. T., Kintner, P. M., ... Holmgren, G. (1992, June). The E-region Rocket/Radar Instability Study (ERRRIS) - Scientific objectives and campaign overview. *J. Atmos. Terr. Phys.*, *54*, 779-808.
- Pfaff, R. F., Sobral, J. H. A., Abdu, M. A., Swartz, W. E., LaBelle, J. W., Larsen, M. F., ... Schmidlin, F. J. (1997, January). The Guara Campaign: A series of rocket-radar investigations of the Earth's upper atmosphere at the magnetic equator. *Geophys. Res. Lett.*, *24*(13), 1663-1666. doi: 10.1029/97GL01534
- Rose, G., Schlegel, K., Rinnert, K., Kohl, H., Nielsen, E., Dehmel, G., ... Neske, E. (1992, June). The ROSE project — Scientific objectives and discussion of first results. *J. Atmos. Terr. Phys.*, *54*, 657-667.
- Samara, M., Michell, R. G., & Khazanov, G. V. (2017, Mar). First optical observations of interhemispheric electron reflections within pulsating aurora. *Geophys. Res. Lett.*, *44*(6), 2618-2623. doi: 10.1002/2017GL072794
- Shkarofsky, J. P., Johnston, T. W., & Bachynski, M. P. (1966). *The Particle Kinetics of Plasmas*. Addison-Wesley, Reading, MA.
- Solomon, S. C., Hays, P. B., & Abreu, V. J. (1988, September). The auroral 6300  emission: Observations and modeling. *J. Geophys. Res.*, *93*(A9), 9867-9882. doi: 10.1029/JA093iA09p09867
- Thorne, R. M., Ni, B., Tao, X., Horne, R. B., & Meredith, N. P. (2010, October). Scattering by chorus waves as the dominant cause of diffuse auroral precipitation. *Nature*, *467*, 943-946. doi: 10.1038/nature09467
- Wiltberger, M., Merkin, V., Zhang, B., Toffoletto, F., Oppenheim, M., Wang, W., ... Stephens, G. K. (2017). Effects of electrojet turbulence on a magnetosphere-ionosphere simulation of a geomagnetic storm. *J. Geophys. Res.*, *122*(5), 5008-5027. doi: 10.1002/2016JA023700